

Geochemistry, Geophysics, Geosystems

RESEARCH ARTICLE

10.1029/2018GC007921

Key Points:

- A 3-D tomographic model of V_p , V_s , and V_p/V_s informs crack aspect ratios in the upper crust at the Endeavour segment, Juan de Fuca Ridge
- Seafloor spreading produces thick cracks with low V_p/V_s , which fill within a few kilometers of the ridge axis by hydrothermal circulation
- Thick cracks on the axis may provide long-lived conduits for hydrothermal upflow beneath the high-temperature vent fields

Supporting Information:

- Supporting Information S1

Correspondence to:

Y. H. Kim,
younghkim@snu.ac.kr

Citation:

Kim, E., Toomey, D. R., Hooft, E. E. E., Wilcock, W. S. D., Weekly, R. T., Lee, S.-M., & Kim, Y. H. (2019). Upper crustal V_p/V_s ratios at the Endeavour segment, Juan de Fuca Ridge, from joint inversion of P and S traveltimes: Implications for hydrothermal circulation. *Geochemistry, Geophysics, Geosystems*, 20, 208–229. <https://doi.org/10.1029/2018GC007921>

Received 6 SEP 2018

Accepted 11 DEC 2018

Accepted article online 15 DEC 2018

Published online 8 JAN 2019

Corrected 6 MAR 2019

This article was corrected on 6 MAR 2019. See the end of the full text for details.

Upper Crustal V_p/V_s Ratios at the Endeavour Segment, Juan de Fuca Ridge, From Joint Inversion of P and S Traveltimes: Implications for Hydrothermal Circulation

Eunyoung Kim¹ , Douglas R. Toomey² , Emilie E. E. Hooft² , William S. D. Wilcock³ , Robert T. Weekly⁴ , Sang-Mook Lee¹, and YoungHee Kim¹ 

¹School of Earth and Environmental Sciences, Seoul National University, Seoul, South Korea, ²Department of Earth Sciences, University of Oregon, Eugene, OR, USA, ³School of Oceanography, University of Washington, Seattle, WA, USA,

⁴Incorporated Research Institutions for Seismology Data Management Center, Seattle, WA, USA

Abstract The Endeavour segment of the Juan de Fuca Ridge is one of the most active and long-lived hydrothermal areas of the mid-ocean ridge system. However, the permeability structure that gives rise to long-term venting at well-established fields, such as the High Rise, Main Endeavour, and Mothra fields, is not fully understood. Here we jointly invert Pg and Sg traveltimes from a seismic refraction experiment conducted at the Endeavour segment using P -to- S coupling constraints. We then calculate porosity and crack density as a function of crack aspect ratio by applying the differential effective medium theory to the seismic velocities. At 1.4-km depth, average V_p ~5 km off axis increases by ~0.4 km/s compared to the ridge axis. The average V_p/V_s has a minimum of ~1.75 on the ridge axis and increases to a maximum of ~1.84 off axis. The inferred porosity and crack density distributions show that the proportion of thick versus thin cracks decreases from the ridge axis to the flanks, since theoretical models indicate that V_p/V_s increases going from thick to thin cracks (aspect ratio decreasing from 0.1 to 0.01). The dominant presence of thick cracks on the axis may provide long-term conduits for upflow in high-temperature hydrothermal circulation potentially forming the vent fields. The increased proportion of thin cracks on the flanks, coupled with the increased seismic velocity, indicates a decrease in permeability caused by progressive clogging of thick cracks due to mineral precipitation likely in the downflow zone of hydrothermal circulation.

1. Introduction

Knowledge of the seismic velocity structure of the oceanic crust is critical to our understanding of the processes of crustal accretion at spreading centers (e.g., Solomon & Toomey, 1992) and the evolution of oceanic crust off axis (e.g., Jacobson, 1992), because seismic velocities are sensitive to composition, porosity, fracture characteristics, temperature, and the presence and distribution of melt. For this reason, numerous marine seismic refraction studies have been conducted over the past 60 years since the pioneering work of Raith (1956). The vast majority reports just the P wave velocity (V_p) structure, employing a variety of forward (e.g., McClain et al., 1985; Purdy & Detrick, 1986) and inverse traveltime modeling techniques (e.g., Bazin et al., 2003; Canales et al., 2003; Hooft et al., 2000; Menke et al., 2002; Seher, Crawford, et al., 2010; Toomey et al., 1994), two- and three-dimensional full-waveform inversions (e.g., Arnoux et al., 2017; Arnulf et al., 2012), and methods to investigate the azimuthal anisotropy of the upper oceanic crust (e.g., Barclay et al., 1998; Dunn & Toomey, 2001; Seher, Crawford, et al., 2010; Sohn et al., 1997; Tong et al., 2004; Weekly et al., 2014).

Studies of S wave velocity (V_s) are more challenging and, thus, less common because S waves are secondary phases that are harder to pick and their presence in marine refraction data depends on the generation of coherent P -to- S converted phases. The formation of a strong P -to- S converted phase requires an interface with a large contrast in seismic properties, and the coherence of the S wave arrivals degrades when the interface is less sharp or is rough on the scales of the seismic wavelength (Spudich & Orcutt, 1980). Nevertheless, additional knowledge of both V_p and V_s provides the V_p/V_s ratio (or Poisson's ratio), which is a powerful indicator of rock lithology and composition (Christensen, 1996; Christensen & Mooney, 1995; Domenico, 1984), melt (Walsh, 1968, 1969) and crack distribution (Collier & Singh, 1998), as well as

the composition and microstructure of magma bodies (Taylor & Singh, 2002). In particular, in the upper oceanic crust both the porosity and the crack morphology affect seismic velocities (Carlson, 2010, 2014a). Theoretical models indicate that the aspect ratios of cracks strongly influence how seismic velocities decrease with increasing porosity and show that the behavior is different for V_p and V_s (Berge et al., 1992; Hudson, 1980). Constraints on both the P and S wave structure are thus useful for inferring the aspect ratio of the cracks that form porosity.

In the 1970s, the development and widespread use of ocean bottom seismometers (OBSs) led to studies of S wave as well as P wave structure beneath the northeast Pacific plate immediately west of Explorer Ridge (Cheung & Clowes, 1981) and the southwest Pacific plate ~1,000 km east of the Tonga Trench (Shearer & Orcutt, 1986). Studies of refracted S waves in relatively young oceanic crust observed low Poisson's ratio (Au & Clowes, 1984; Spudich & Orcutt, 1980) that may be related to the aspect ratios of water-filled cracks within rock (Shearer, 1988). In 1973 and 1979, seismic refraction studies were conducted on the flanks of the Mid-Atlantic Ridge (MAR; Fowler, 1976) and the East Pacific Rise (EPR; Bratt & Solomon, 1984), respectively, to analyze S wave structure.

In the past few decades, only a few seismic experiments have been able to constrain S wave structure near oceanic spreading centers. At the EPR, V_s profiles in the crust were constrained using traveltimes inversion, forward waveform modeling, and the reflectivity analysis of expanded spread profiles data (Vera et al., 1990). Poisson's ratio, which is related to V_p/V_s , for young oceanic crust was constrained using amplitude modeling of seismic refraction data obtained by placing both the source and receiver close to the seafloor (Christeson et al., 1994). The 1-D full waveform inversion of wide-aperture profiles data using reflected and refracted/turning ray arrivals (Collier & Singh, 1998) and 1-D waveform inversion of refracted arrivals from OBS data (Christeson et al., 1997) were also used to model the Poisson's ratio structure of the upper crust. At the MAR, microearthquake arrival time data were jointly inverted for hypocenters and 1-D P and S wave velocity structures (Barclay et al., 2001). At the Endeavour segment of the Juan de Fuca Ridge (JdFR), a joint inversion of shots and earthquake traveltimes was used to constrain 1-D V_s and V_p/V_s structures within the on- and off-axis regions (Barclay & Wilcock, 2004). Seafloor compliance techniques were also used to determine the V_s profile and provide constraints in V_p/V_s both on and off axis at the EPR (Crawford et al., 1999; Hulme et al., 2003). In addition, shear wave splitting was observed in microearthquake data from the west flank of the southern EPR (Hung & Forsyth, 1999), the Endeavour segment of the JdFR (Almendros et al., 2000), and the axis of the MAR near 35°N (Barclay & Toomey, 2003). In these studies, the time delays between fast and slow S wave arrivals were interpreted as an effect of upper crustal anisotropy due to vertical, fluid-filled cracks aligned parallel to the ridge axis.

In this paper, we jointly invert crustal refraction traveltimes of P and S wave arrivals obtained from a seismic refraction experiment carried out in 2009 at the Endeavour segment of the JdFR to obtain a three-dimensional model of V_p and V_s in the upper crust. This is the first three-dimensional model of V_s obtained in the oceanic crust. We also calculate models of V_p , V_s , and V_p/V_s for a cracked medium with variable porosity and crack aspect ratios using differential effective medium (DEM) theory (Bruner, 1976; McLaughlin, 1977) and use these to interpret the velocity structure and in particular the V_p/V_s ratio, in terms of spatial variations in the distribution and nature of cracks. We discuss the implications for tectonic and hydrothermal processes that act to create and seal cracks.

2. Geologic Setting

The Endeavour segment is a 90-km-long spreading center located near the northern end of the JdFR (Figure 1a) with an intermediate full-spreading rate of 52 mm/year (DeMets et al., 2010). At its north and south ends, the Endeavour segment forms the Endeavour-West Valley and the Cobb overlapping spreading centers (OSCs) with the West Valley and Northern Symmetric segments, respectively (Figure 1a). The central portion of the segment is elevated relative to the segment ends and hosts five major hydrothermal vent fields spaced 2 to 3 km apart, named from north to south, Sasquatch, Salty Dawg, High Rise, Main Endeavour, and Mothra (Figure 1b; Delaney et al., 1992; Kelley et al., 2001; Robigou et al., 1993). The heat source for vigorous hydrothermal circulation is an axial magma chamber (AMC) that extends ~24 km along axis (Van Ark et al., 2007). The top of the AMC lies at 2.1- to 3.3-km depth and is shallowest beneath the hydrothermal fields.

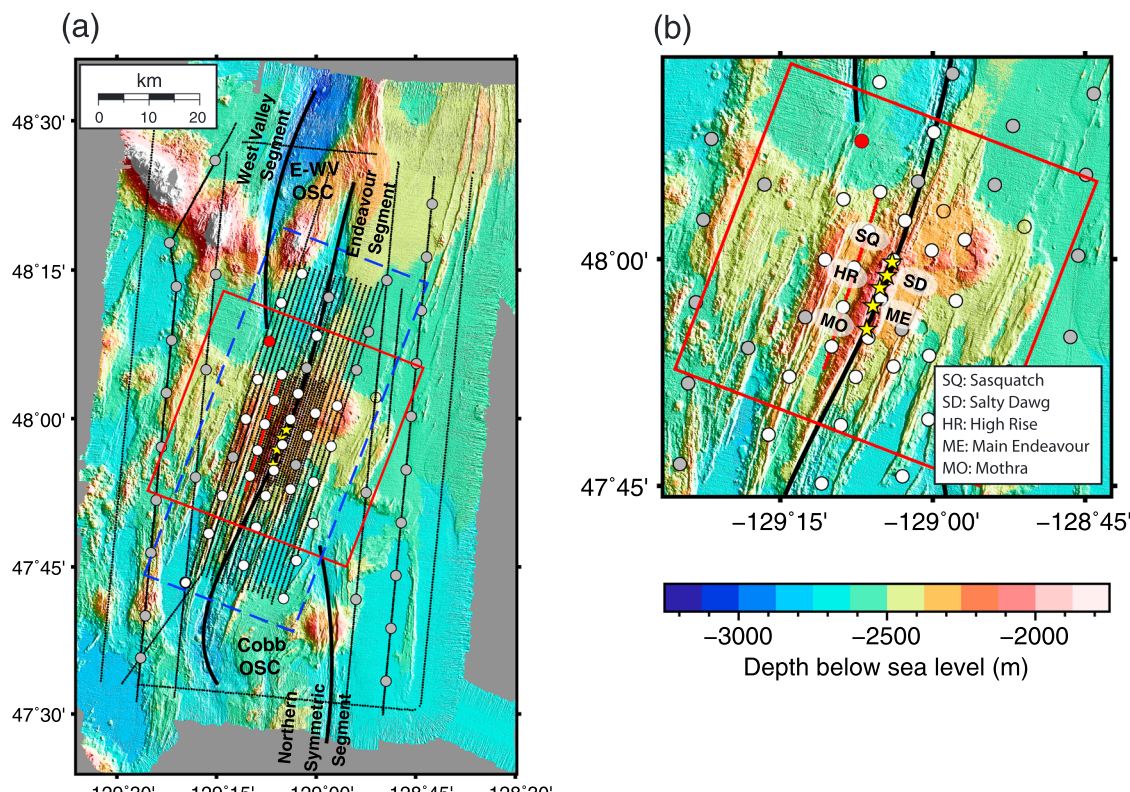


Figure 1. Map of the Endeavour tomography seismic experiment at the Endeavour segment of the Juan de Fuca Ridge. (a) The white circles indicate OBSs that are used to pick both Sg and Pg phases. The gray circles indicate OBSs used to pick only Pg. The OBSs that did not record data are shown by open circles. The air gun shots (black dots) have average shot spacing of 450 m along all lines. The red symbols indicate the OBS and shots for the record sections in Figure 2. The bold black lines indicate the West Valley, Endeavour, and Northern Symmetric segments of the plate boundary. The northern and southern ends of the Endeavour segment form the Endeavour-West Valley (E-WV) and Cobb OSCs, respectively. The dashed blue box encloses the nineteen 60-km-long lines of the crustal grid and is the area ($30 \times 70 \text{ km}^2$) of map views shown in Figure 4. The red box shows the central area ($40 \times 40 \text{ km}^2$) of the Endeavour segment used to calculate the mean values of velocities and anisotropy as a function of distance from the ridge axis in Figure 8. (b) Enlarged bathymetric map showing the locations of high-temperature vent fields (yellow stars). SQ = Sasquatch; SD = Salty Dawg; HR = High Rise; ME = Main Endeavour; MO = Mothra.

Segment-scale tomographic images of upper crustal P wave velocity structure show that V_p is generally higher beneath the segment center than to the north and south, presumably reflecting increased fracturing in the regions impacted by the OSCs (Weekly et al., 2014). Layer 2A thickness varies between 180 and 630 m along axis, thickening systematically south of the central axial high compared to the north (Van Ark et al., 2007). The P wave structure of the central 30–40 km of the Endeavour is characterized by alternating ridge-parallel bands of high- and low-velocity anomalies (Arnoux et al., 2017; Barclay & Wilcock, 2004; Weekly et al., 2014) that are ~4 km wide and extend 10–12 km to either side of the axis. The low-velocity bands lie beneath the outer flanks of off-axis abyssal hills and are attributed to the thickening of the extrusive layer by eruptions flowing off the axial high (Arnoux et al., 2017; Weekly et al., 2014). This interpretation is generally consistent with multichannel seismic data, which show that layer 2A is on average thicker below bathymetric highs (Van Ark et al., 2007).

The Endeavour segment is seismically active (Hooft et al., 2010; Weekly et al., 2013; Wilcock et al., 2002, 2009). In 2003–2004, the rate of seismicity was particularly high between the Main Endeavour and High Rise fields (Wilcock et al., 2009), which are the fields with the largest number of black smoker vents, the highest maximum venting temperatures (Kelley et al., 2002), and the highest heat fluxes of several hundred megawatts (Kellogg, 2011). Here earthquake focal mechanisms are consistent with inflation of the AMC, leading Wilcock et al. (2009) to infer that magma injection provides a critical mechanism to thin the conductive boundary layer and maintain heat fluxes. P wave velocities just above the AMC are also lower beneath

the Main Endeavour and High Rise fields than other fields (Arnoux et al., 2017; Weekly et al., 2014) consistent with increased rates of earthquake-induced fracturing.

At the Endeavour, one-dimensional models of S wave velocities on and off axis were previously obtained by the joint inversion of microearthquake data obtained from a 2-month experiment in 1995 and ~50 small explosive shots deployed during the experiment to locate the OBS network (Barclay & Wilcock, 2004). Based on studies at other mid-ocean ridge sites (Barclay et al., 2001; Collier & Singh, 1998) and the timing of *P*-to-*S* and *S*-to-*P* conversions at the base of layer 2A observed on earthquake record sections for the Endeavour (Wilcock et al., 2002), the *Vp/Vs* ratio was set to 2.9 at depths \leq 0.25 km, while a value of 1.8 was assumed at depths \geq 0.5 km. The inversion yielded $Vp/Vs = 1.8\text{--}1.9$ (equivalent to a Poisson's ratio $\sigma = 0.28\text{--}0.31$) at depths \geq 1 km both on and off axis (Barclay & Wilcock, 2004). At depths between 0.5 and 1 km, *Vp/Vs* increased from 1.8 ($\sigma = 0.28$) on axis to 1.95 ($\sigma = 0.32$) off axis, which was attributed to an artifact of the limited resolution of the inversion or preferential sealing of thin cracks by hydrothermal processes (Barclay & Wilcock, 2004).

3. Data and Methods

3.1. Endeavour Tomography Experiment

The Endeavour tomography experiment was conducted in 2009 to image the three-dimensional seismic velocity structure from the topmost mantle to the shallow crust beneath the Endeavour segment. Sixty-eight four-component (three orthogonal geophones and a hydrophone channel) OBSs were deployed at 64 sites to record ~5,500 air gun shots from the 36-element, 6,600-in.³ air gun array of the R/V *Marcus G. Langseth*. Air gun data were collected along 2,500 km of track line at a typical shooting interval of 180 to 210 s (average shot spacing of 450 m). The source-receiver distribution has a nested geometry with an area of approximately 90 km along axis and 60 km across axis. At the segment scale, the data resolve the nature of sub-ridge mantle flow and the pattern of melt transport from the topmost mantle to crust (VanderBeek et al., 2016) and the crustal thickness and lower crustal velocity (Soule et al., 2016). At the crustal scale, the data constrain the on- and off-axis velocity structure and the along-axis character of the shallow crustal architecture (Weekly et al., 2014). At a detailed scale around the vent fields, full-waveform inversion revealed the structure associated with hydrothermal circulation between the magmatic system and the seafloor (Arnoux et al., 2017).

Instrument and shot locations were determined simultaneously by inverting acoustic-water-wave arrivals (Creager & Dorman, 1982). For stations and shots, the horizontal 1σ location uncertainties were 13 and 9 m, respectively. Vertical station uncertainty was 10 m, as determined from the bathymetric map obtained using the onboard EM122 multibeam system. The *P* wave crustal refraction (*Pg*) phase data (Figure 2b) was picked on 62 instruments (Weekly et al., 2014). The *Pg* data include 97,302 traveltimes and have a root-mean-square (RMS) uncertainty of 13 ms.

3.2. *Sg* Traveltime Data Set

The *S* wave crustal refraction (*Sg*) phase was picked on 31 OBSs with two good horizontal components for shots along the nineteen 60-km-long lines within the crustal grid (Figure 1a). Since the OBSs are free-fall instruments, the orientations of the horizontal components were determined from the shot-receiver azimuth and the observed direction of horizontal particle motion of the water wave arrivals (Bratt & Solomon, 1984; Tréhu, 1984). We pick *Sg* arrivals after resolving the horizontal channels into the radial direction (red picks in Figure 2a) because most converted energy from the compressive marine sound source is in this direction.

In the oceanic crust, the *P*-to-*S* conversion occurs where the seismic wave encounters a large velocity contrast (White & Stephen, 1980). At the Endeavour segment, there is almost no sediment layer within 20 km of the ridge axis (Nedimović et al., 2008). In young oceanic crust a thin surficial low-velocity (<3.0 km/s), low-gradient layer, layer 2A, is underlain by a high-gradient region, where velocities of >5 km/s are reached at a depth of ~200–600 m beneath the seafloor in seismic layer 2B (Christeson et al., 1994; Harding et al., 1989; Vera et al., 1990). Christeson et al. (1997) found that at the EPR, the *P*-to-*SV* conversion is negligible at the seafloor and that for upgoing rays, amplitudes of *S*-to-*S* transmission are larger than for *S*-to-*P* conversion at the 2A/2B interface. Consequently, at the mid-ocean ridge *P*-to-*S* conversion mainly occurs on the downgoing path in the high-gradient region at the base of layer 2A (Christeson et al., 1997).

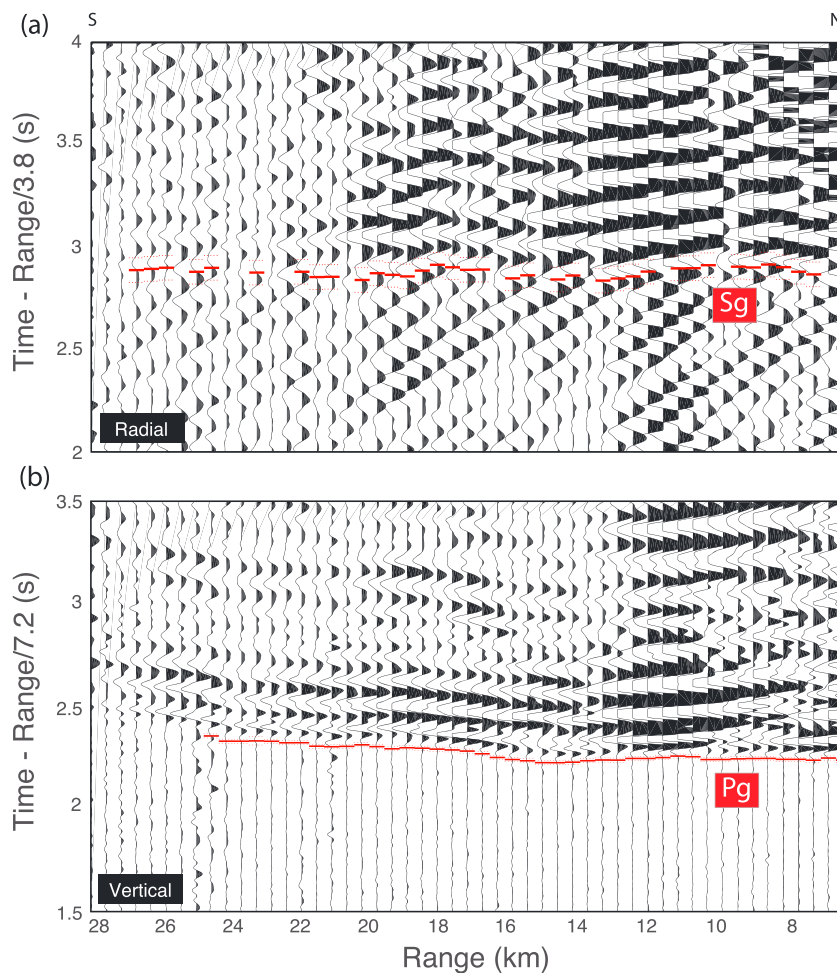


Figure 2. Example radial and vertical record sections for OBS 62 and the shot line shown as red symbols on Figure 1. (a) Sg picks (red ticks) on the radial channel formed by orienting the two horizontal channels and rotating into the radial direction. (b) Pg picks (red ticks) on the vertical channel. Waveform data are band-pass filtered between 5 and 25 Hz. Record sections are plotted with reduction velocities of 3.8 and 7.2 km/s on the radial and vertical channels, respectively.

In horizontal record sections, we observe coherent phases of S wave with apparent velocities of $\sim 3.5\text{--}4.0$ km/s (Figure 2a). Unlike Pg, the Sg phase is a secondary arrival and it is thus more difficult to pick arrival times precisely (Figures 2 and supporting information Figure S1). We first identify Sg arrivals using trace-to-trace coherency of phases with apparent velocities of ~ 3.5 km/s on a larger-scale record section plotted with a velocity reduction of 7.2 km/s (Figure S1). Most Sg phases are identified at ranges of 6–30 km with some arrivals picked to a maximum range of 36 km. On the seismogram, the Sg first motion is in the receiver-to-source direction (to the left on our record sections), followed by a larger motion in the opposite direction (Figure 2a). Because it is easier to see the coherency of Sg phase on the larger-amplitude oscillation, we pick the larger Sg phase associated with the onset of the second half of the cycle and then adjust the time so that it matches the initial onset of the arrival where that is visible. We adopt the following iterative strategy to reduce the picking error and obtain as many Sg traveltimes as possible. We first handpick those Sg arrivals with good trace-to-trace coherency on non-ridge crossing shot lines and invert only Sg data for a smooth Vs model. Using this velocity model, we predict Sg traveltimes and use these synthetic picks as a guide to identify more arrivals that have weaker signal-to-noise or trace-to-trace coherency. The Sg picks with large residuals are reviewed, and the data are inverted again after removal of outliers. Since the quality of the Sg arrivals is not consistent at all receivers, this picking procedure is repeated until we have confidence in our Sg data. When the picking is complete, we simultaneously invert our Sg data with the Pg data of Weekly

Table 1
Matrix Components and Parameters Used for Joint Inversion

Parameter	Description
G	Fréchet derivatives for slowness parameters
d	Vector of the differences between observed and calculated traveltimes
m	Vector of perturbations to model parameters
$\Delta \mathbf{u}_P$	Isotropic P wave slowness perturbations
$\Delta \mathbf{u}_S$	Isotropic S wave slowness perturbations
C_d	Diagonal matrix of data variance composed of the squares of data uncertainties
C_p	Diagonal matrix of the a priori P wave model variance
C_s	Diagonal matrix of the a priori S wave model variance
C_{PS}	Matrix of coupling constraint between P and S slowness perturbations
C_{PH}	Matrix of horizontal Gaussian smoothing for P slowness model parameter
C_{PV}	Matrix of vertical Gaussian smoothing for P slowness model parameter
C_{SH}	Matrix of horizontal Gaussian smoothing for S slowness model parameter
C_{SV}	Matrix of vertical Gaussian smoothing for S slowness model parameter
Weighting parameters used to specify the relative importance of each constraint	
$\lambda_P = 1$	P wave slowness model norm
$\lambda_S = 1$	S wave slowness model norm
$\lambda_{PS} = 100$	P-to-S coupling constraint
$\lambda_{PH} = 300$	P wave slowness horizontal smoothing
$\lambda_{PV} = 200$	P wave slowness vertical smoothing
$\lambda_{SH} = 100$	S wave slowness horizontal smoothing
$\lambda_{SV} = 100$	S wave slowness vertical smoothing

et al. (2014). The final Sg data set includes 4,205 picks with uncertainties of 30–80 ms that are visually estimated on the basis of the signal-to-noise ratio and trace-to-trace coherency.

3.3. Tomographic Method

We use an iterative inversion method (Toomey et al., 1994) in which the *P*-to-*S* coupling constraint is applied to the relative *P* and *S* slowness perturbations (Hammond & Toomey, 2003). The forward problem is solved using a shortest-path ray tracing method (Moser, 1991) to predict raypaths and traveltimes of an initial model. We solve the forward problem for Pg and Sg arrivals separately because their raypaths are not the same when V_p/V_s varies. Since Sg arrivals are converted at the bottom of layer 2A from *P* waves downgoing beneath the seafloor, they propagate as *P* waves in layer 2A until the conversion. However, our ray tracing method assumes that Sg arrivals travel as *S* waves along the entire crustal path. The predicted Sg traveltimes are thus larger than the data by the traveltime difference between *S* and *P* wave in the layer 2A. To account for this overestimate, we use the results of a previous study to adjust the predicted Sg traveltimes. In a seismicity study from the Endeavour segment, a secondary arrival at a constant delay of just over 0.4 s relative to the *P* arrival and a weak phase 0.4 s before the *S* wave were interpreted as a *P*-to-*SV* conversion and *SV*-to-*P* conversion, respectively, at the base of layer 2A (Wilcock et al., 2002). These observations provide an estimate of the difference between the predicted and the observed Sg traveltime, which is applied by adding 0.4 s to the observed times.

The inverse problem for seismic tomography is ill-conditioned, and it is often regularized by applying model norm and spatial smoothing constraints. In addition, since the *P* wave traveltime data set is generally much larger and has a higher quality than the *S* wave data set, the V_s

model is less well constrained. To account for this difference in resolving power, we also impose *P*-to-*S* coupling constraints in order to stabilize the inversion for V_p/V_s .

The nonlinear tomographic inverse problem is solved for changes to the starting model. We apply conditions of minimum model norm, spatial smoothing, and *P*-to-*S* coupling as follows

$$\begin{bmatrix} \mathbf{G} \\ \lambda_p \mathbf{C}_P \\ \lambda_s \mathbf{C}_S \\ \lambda_{PS} \mathbf{C}_{PS} \\ \lambda_{PH} \mathbf{C}_{PH} \\ \lambda_{PV} \mathbf{C}_{PV} \\ \lambda_{SH} \mathbf{C}_{SH} \\ \lambda_{SV} \mathbf{C}_{SV} \end{bmatrix} \begin{bmatrix} \Delta \mathbf{u}_P \\ \Delta \mathbf{u}_S \end{bmatrix} = \begin{bmatrix} \mathbf{d} \\ \mathbf{0} \end{bmatrix}. \quad (1)$$

Solving this set of equations is equivalent to minimization of the following functional

$$s^2 = \mathbf{d}^T C_d^{-1} \mathbf{d} + \lambda_p \mathbf{m}^T C_p^{-1} \mathbf{m} + \lambda_s \mathbf{m}^T C_s^{-1} \mathbf{m} + \lambda_{PS} \mathbf{m}^T C_{PS}^{-1} \mathbf{m} + \lambda_{PH} \mathbf{m}^T C_{PH}^{-1} \mathbf{m} + \lambda_{PV} \mathbf{m}^T C_{PV}^{-1} \mathbf{m} + \lambda_{SH} \mathbf{m}^T C_{SH}^{-1} \mathbf{m} + \lambda_{SV} \mathbf{m}^T C_{SV}^{-1} \mathbf{m}, \quad (2)$$

where each parameter is described in Table 1.

Since independent inversions for V_p and V_s can yield unphysical models, especially in V_p/V_s structure, it is useful to constrain the relationship between V_p and V_s . Imposing a *P*-to-*S* coupling constraint assumes that V_s correlates with V_p , which indicates that their ratio may be a more smoothly varying medium property

Table 2
Three Types of P-to-S Coupling Tested to Determine the Proper Constraint

Type A	Type B	Type C
Smooth $\delta\left(\frac{V_p}{V_s}\right)$ $\delta\left(\frac{V_p}{V_s}\right) = \frac{V_s \delta V_p - V_p \delta V_s}{V_s^2}$ $= \frac{u_p \delta u_s - u_s \delta u_p}{u_p^2}$ <p>and spatially average</p> $\delta\left(\frac{V_p}{V_s}\right)_i = \sum_{j \neq i} w_j \delta\left(\frac{V_p}{V_s}\right)_j$	Constant $\frac{\partial \ln V_s}{\partial \ln V_p}$ $\frac{\partial \ln V_s}{\partial \ln V_p} \approx \frac{V_p}{V_s} \frac{\Delta V_s}{\Delta V_p}$ $= \frac{u_p}{u_s} \frac{\Delta u_s}{\Delta u_p}$ $= \text{constant}$	Unchanged from starting V_p/V_s Starting V_p/V_s 3.35 1.80 Depth ≤ 0.4 km ≥ 0.6 km
		^a w_j is the Gaussian weights with a characteristic length equal to the node spacing (Toomey et al., 1994).

than V_s itself (Brocher, 2005; Eddy et al., 2013). To constrain the relationship between P and S slowness perturbations during the inversion, we evaluate three types of P -to- S coupling constraints (Table 2; Hammond & Toomey, 2003). Type A assumes that the V_p/V_s variation is spatially smooth. Type B assumes that $\partial \ln V_s / \partial \ln V_p$, the ratio of the fractional changes in V_s and V_p , is constant at all perturbation nodes. In type C, the V_p/V_s ratio is constrained to be smooth relative to the starting model. In each instance, the strength of the constraint is controlled by a P -to- S coupling parameter.

The ratio of the fractional changes in V_s and V_p , $\partial \ln V_s / \partial \ln V_p$, has been mainly used as an assumption in the inversion for V_p and V_s of the mantle (Hammond & Toomey, 2003; Masters et al., 1982; Woodward & Masters, 1992). For the solid upper mantle, $\partial \ln V_s / \partial \ln V_p$ is expected to vary between 0.9 and 1.6 on the basis of thermodynamic arguments (Anderson & Isaak, 1995), and it may be as high as 2.2 for partially molten rocks. For oceanic crust, particularly in the upper crust, we expect that fluid-filled cracks are the dominant control on seismic velocity. We thus test $\partial \ln V_s / \partial \ln V_p$ values between 0.8 and 2.2, which are appropriate for the crack aspect ratio of a rock-water system near 0-km depth as inferred from seismic observations by Takei (2002).

3.4. DEM Theory

Seismic velocities in the upper oceanic crust are affected considerably by variations in crack morphology and porosity (Carlson, 2010, 2014a; Swift et al., 2008). Alteration of the primary mineral phases also affects seismic velocities, but the effect is relatively small. The grain velocities in basalt and diabase samples from Hole 504B show that alteration only reduces velocities by ~0.2 km/s (Carlson, 2014b). In contrast, lava cracks at the scale of rock samples and cracks at large scales reduce the average in situ velocity by ~1.1 and ~1.7 km/s, respectively (Carlson, 2014b). Since cracks account for nearly 90% of the difference between in situ and the theoretical seismic velocities in the upper crust (Carlson, 2014b), an understanding of the effects of the crack density and the distribution of crack aspect ratios on seismic velocities is important to interpret the results of seismic refraction experiments.

The effects of porosity and crack aspect ratios on V_p and V_s can be estimated using two forms of effective medium theory. For the DEM method (Bruner, 1976; McLaughlin, 1977), the elastic moduli at a given volume fraction of inclusions, such as grains or cracks, is evaluated by adding inclusions incrementally into a background medium. For the self-consistent (SC) method (Budiansky, 1965; Hill, 1965), the average elastic tensor of all crystals in the aggregate is estimated in one step. A combination of the SC and DEM has been used to model the effective elastic properties of shales (Hornby et al., 1994), hydrate-bearing sediments (Jakobsen et al., 2000), and partially molten rocks at mid-ocean ridges (Mainprice, 1997). However, velocities of rocks such as basalts, which have isolated cracks and pores, can be better estimated using the DEM than the SC method (Berge et al., 1993). Thus, we perform DEM modeling to calculate the effective elastic properties of a composite of basalt and seawater-filled cracks and to predict the relationship between velocity and porosity. We assume that the nature of the porosity is independent of depth, thus ignoring possible changes in pore geometry between pillows/flows/sills and the dike section (Seher, Singh, et al., 2010).

The tensor equation for the DEM method (McLaughlin, 1977) is as follows:

$$\frac{dC}{dv_i} = \frac{1}{1 - v_i} (C_i - C) Q_i, \quad (3)$$

where dC is the change in the elastic moduli of the effective medium due to an increment dv_i at a given volume fraction v_i (or porosity) of the inclusion phase with elastic stiffness tensor C_i . The term Q_i is the strain concentration factor coming from the Eshelby formulation of the inclusion problem (Mainprice, 1997) given as

$$Q_i = [I + G(C_i - C)]^{-1}, \quad (4)$$

where G is the symmetrical fourth-rank tensor Green's function that is calculated from the response of a single inclusion embedded in a matrix of the effective medium (Eshelby, 1957; Mura, 1987). It is assumed that individual inclusion may be approximated by an ellipsoid

$$\frac{x_1^2}{a_1^2} + \frac{x_2^2}{a_2^2} + \frac{x_3^2}{a_3^2} \leq 1. \quad (5)$$

In our DEM model, the effective medium consists of two components of basalt and seawater-filled crack as a host and inclusion, respectively. The physical properties of components are $V_p = 6.4$ km/s, $V_s = 3.5$ km/s, and density $\rho = 2,971$ kg/m³ for basalt (Johnston & Christensen, 1997), and $V_p = 1.5$ km/s, $V_s = 0$ km/s, and $\rho = 1,030$ kg/m³ for seawater (Telford & Sheriff, 1990). The inclusions are introduced in an aligned manner since the seismic anisotropy in the upper oceanic crust is attributed to vertical cracks aligned parallel to the ridge axis (Stephen, 1985). All inclusions lie parallel with their a_3 axis along the x_3 direction and $a_1 = a_2$ so that the effective medium is transversely isotropic with the x_1 and x_2 directions being equivalent. For Cartesian coordinates, x_1 , x_2 , and x_3 directions are vertical, parallel, and perpendicular, respectively, to the ridge axis. For a transversely isotropic material, the nonzero elastic stiffness components are $c_{11} = c_{22}$, c_{33} , $c_{44} = c_{55}$, c_{66} , $c_{13} = c_{23}$, and $c_{12} = (c_{11} - 2c_{66})$ (Musgrave, 1970). The elastic stiffness components from the DEM are converted to the velocities in fast (x_1 and x_2) and slow (x_3) directions (Jakobsen et al., 2000);

$$\text{Fast } V_p = \sqrt{c_{11}/\rho}, \quad (6)$$

$$\text{Slow } V_p = \sqrt{c_{33}/\rho}, \quad (7)$$

$$\text{Fast } V_s = \sqrt{c_{66}/\rho}, \quad (8)$$

$$\text{Slow } V_s = \sqrt{c_{44}/\rho}. \quad (9)$$

We use the DEM theory to predict V_p and V_s in the slow direction in the upper oceanic crust as a function of porosity assuming aligned cracks. We model the slow direction because refracted seismic rays travel approximately horizontally for the majority of the raypath. Since the DEM theory assumes all inclusions have a constant aspect ratio, we obtain multiple solutions assuming a range of crack aspect ratios (Figure 3). For small aspect ratios, the modeled V_s and V_p at low porosities both decrease rapidly as porosity is increased, but the dependence of the rate of decrease on the aspect ratio is different. As the crack aspect ratio decreases from 0.02 to 0.005, the rate at which V_s decreases with porosity increases (Figure 3b), whereas V_p decreases at a similar rate (Figure 3a). As a result, V_p/V_s increases very rapidly with porosity for the smallest crack aspect ratios (Figure 3c). In contrast, for crack aspect ratios of 0.5 to 0.1, V_s decreases more slowly with porosity and is less sensitive to crack aspect ratio than V_p (Figures 3a and 3b). This leads to V_p/V_s decreasing with porosity for fatter cracks (Figure 3c). The different effects of crack aspect ratio on elastic properties are very pronounced in Poisson's ratio (Figure 3d). Cracks with aspect ratios of 0.005–0.02 act to increase Poisson's ratio, whereas cracks with aspect ratios of 0.1–0.5 decrease Poisson's ratio (Figure 3d).

4. Tomographic Analysis

4.1. Starting Model and V_p/V_s Coupling

The tomographic analysis requires initial V_p and V_s models. The initial V_p model is taken from the Pg traveltime tomography results of Weekly et al. (2014). The starting V_s model is derived from the V_p model

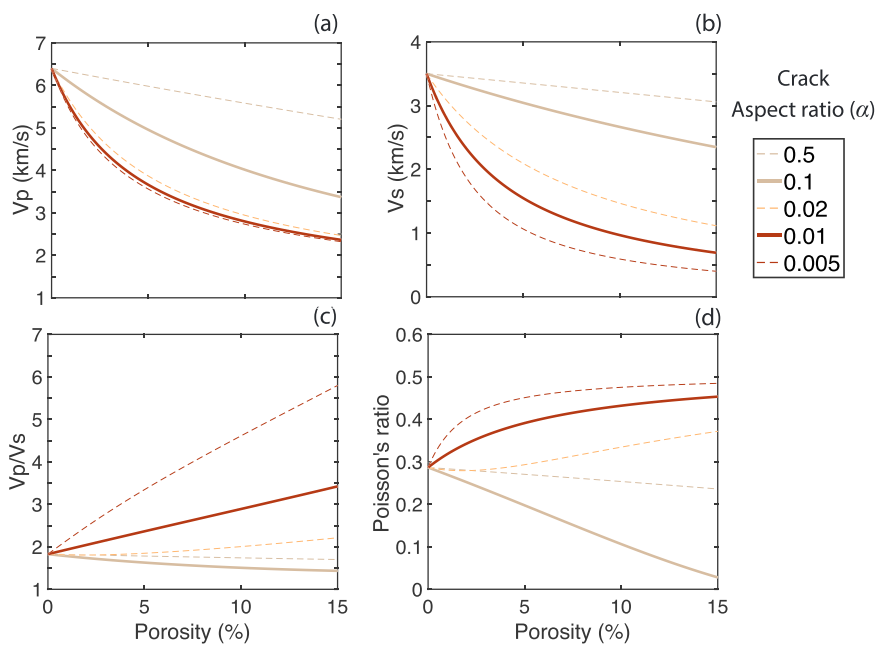


Figure 3. Estimates of (a) V_p , (b) V_s , (c) V_p/V_s , and (d) Poisson's ratio as a function of porosity for various crack aspect ratios (colored lines) using the differential effective medium theory. The cracks are assumed to be vertically aligned ellipsoids, and V_p and V_s are shown for the slow direction. The effective medium of a two-phase composite consists of a basalt host ($V_p = 6.4$ km/s; $V_s = 3.5$ km/s; density = $2,971$ kg/m 3 ; Johnston & Christensen, 1997) and seawater inclusions ($V_p = 1.5$ km/s; $V_s = 0$ km/s; density = $1,030$ kg/m 3 ; Telford & Sheriff, 1990).

assuming V_p/V_s ratios for layers 2A and 2B. The seismic properties in layer 2A are not fully constrained by our data because all the rays travel along near-vertical paths through it. Layer 2A acts to introduce a static offset to traveltimes that constrains only the product of the thickness and slowness in the layer and which in inversions can be partitioned. Weekly et al. (2014) parameterized layer 2A in the starting model for the inversions for P wave structure as a layer with low velocities of ~ 2.5 km/s at model grid depths of 0 and 0.2 km that transitioned to layer 2B velocities at 0.4-km depth. We adopted the same approach for our S wave model and forward modeled the S wave data using the three-dimensional P wave model of Weekly et al. (2014) and various choices of V_p/V_s ratios in layer 2A and the crust beneath (layer 2B). We find that for a value of $V_p/V_s = 1.8$ in layer 2B, the mean of the Sg misfits is 0 for $V_p/V_s = 3.35$ in layer 2A, while for $V_p/V_s = 1.9$ in layer 2B, the mean of the Sg misfits is 0 for $V_p/V_s = 2.6$ in layer 2A. We chose a starting model with $V_p/V_s = 3.35$ at model grid depths of 0–0.4 km and $V_p/V_s = 1.8$ at depths ≥ 0.6 because this choice predicts an S minus P travelttime delay of 0.4 s through layer 2A, which is consistent with that observed for P -to- S and S -to- P converted phases that form at the base of layer 2A in microearthquake records (Wilcock et al., 2002). We note that since our parameterization has an effective layer 2A thickness of 0.3 km (i.e., a transition that occurs between the 0.2- and 0.4-km deep nodes) while the mean layer 2A thickness on the Endeavour is about 0.4 km (Van Ark et al., 2007), the V_p/V_s in layer 2A is likely somewhat lower than 3.35.

A series of inversions were performed to explore P -to- S coupling, and, for appropriate smoothing and coupling weights, we found that the results are very similar for all three types of coupling. The RMS of Pg residuals was effectively constant at 11 ms for all coupled inversions, while the RMS of Sg increased for all coupling types as the horizontal (λ_{SH}) and vertical (λ_{SV}) smoothing weights for V_s increased. The results were not very sensitive to the type of coupling. For example, type A with coupling weight of 1 and type B with coupling weight of 100 resulted in similar models that both fit Sg data well. Since similar results were obtained for all three types of coupling, we infer that the data require a heterogeneous V_p/V_s structure. Our preferred solution uses type B coupling, which attempts to keep the $\partial \ln V_s / \partial \ln V_p$ ratio constant, and a coupling weight of 100; smaller values of coupling resulted in larger fluctuations of V_p/V_s . We also found that the results were insensitive to the chosen value of $\partial \ln V_s / \partial \ln V_p$, and so a value (1.1) that corresponds to that of rock including water-filled cracks with aspect ratio of 0.02 is used (Takei, 2002).

4.2. Tomographic Resolution

We investigated ray coverage and reconstructed several synthetic models to evaluate the resolution of our tomographic results. The spatial distribution of Sg raypaths is indicated by the derivative weight sum (Toomey et al., 1994; Figure S2) and shows good coverage of the Vs model in a region $15 \times 40 \text{ km}^2$ centered on the Salty Dawg vent field. For all synthetic models, we calculated Pg and Sg traveltimes using the same shot-receiver pairs as in our experiment, assigned uncertainties of 10 and 60 ms, respectively, and inverted using the same parameters as in our preferred models.

To evaluate model resolution at the segment scale, we constructed synthetic models with horizontal and vertical checkerboard-patterned velocity anomalies (Figures S3 and S4). For the horizontal checkerboard test (Figure S3), the true model consists of cylindrical anomalies with a sinusoidal pattern of wavelength 4 km in the XY plane with a peak amplitude of 5% superimposed on the 3-D starting model. To investigate vertical resolution, we generated a synthetic model with 2-km cubes beneath the across-axis profile at the High Rise vent field (Figure S4). Velocity perturbation of $\pm 5\%$ was superimposed on the 3-D starting Vp and Vs models. In both cases the checkerboard anomalies of Vp and Vs are well recovered in the upper 3 and 2 km, respectively (Figures S3 and S4). The recovered amplitude of Vs anomalies is poorer than Vp between 1- and 3-km depths (Figures S3 and S4), reflecting the small percentage of Sg raypaths turning at these depths. A low Vs anomaly beneath the ridge axis at depths between 2 and 3 km is not recovered (Figure S4), whereas low Vs anomalies beneath the flanks (within 5–10 km from the ridge axis) at these depths are recovered, although the magnitudes are underestimated.

When the magnitudes and polarities of perturbation are the same for both Vp and Vs, the perturbation of Vp/Vs is 0. Thus, we conducted additional synthetic tests to investigate the ability of Vp/Vs resolution in our joint inversion by reconstructing more geologically plausible anomalies. We constructed synthetic Vs models containing several spheroidal Vp/Vs anomalies with a diameter of 2.4 km distributed across the ridge axis beneath each hydrothermal vent field profile (Figure S5). The Vp/Vs perturbation of all anomalies is 0.3 with respect to a model with a constant Vp/Vs ratio at each depth. The locations of recovered anomalies beneath all hydrothermal vent fields are resolved in the upper 2 km except beneath the Sasquatch field in the north (Figure S5). However, the magnitudes of the low- and high-Vp/Vs anomalies are underestimated (Figure S5). We conclude that the locations and overall form of Vp/Vs variations observed in our preferred tomographic solution are robust features and that Vp/Vs anomalies as small as ~2 km in diameter are resolved by our Pg and Sg data sets. However, the resolution tests indicate that the magnitude of Vp/Vs variations is likely underestimated.

4.3. Tomographic Results

The upper crustal velocity structure of the Endeavour segment is very heterogeneous. Figure 4 shows map view sections of Vp, Vs, and Vp/Vs perturbations relative to the horizontal average at 0.4-, 1.4-, and 2.4-km depths. The preferred Vp model mirrors that obtained from prior inversions of just P wave arrival times (Weekly et al., 2014) and is thus not significantly perturbed from the starting model. In contrast, Vs is perturbed from the starting model leading to substantial horizontal variations in Vp/Vs to simultaneously fit the Pg and Sg arrival times (Figures 4g–4i).

At the segment scale, Vp is lower at the segment ends near the Endeavour-West Valley and Cobb OSCs than in the central part of the segment at all depths (Figures 4a–4c). At depths $\leq 1.4 \text{ km}$, the segment center is characterized by alternating bands of high and low Vp (Figures 4a and 4b). Off axis, the amplitudes of low-Vp bands gradually decrease with increasing depth, which is accompanied by an increase in Vp off axis at $> 1.2 \text{-km}$ depth. Vs tends to be lower at all depths near the OSCs than in the segment center (Figures 4d–4f), although the ray density at the segment ends is low (Figures S2a–S2e) and not all the area of OSCs are imaged. The fractional amplitudes of Vs anomalies at the segment ends tend to be lower than those for Vp at depths $> 0.4 \text{ km}$ (Figures 4e and 4f) leading to positive Vp/Vs anomalies (Figures 4h and 4i). Conversely, at the segment center, Vs anomalies near the ridge axis tend to be greater than Vp anomalies at depths $> 0.4 \text{ km}$ (Figures 4e and 4f) leading to negative Vp/Vs anomalies (Figures 4h and 4i). The banded high- and low-velocity anomalies near the segment center are apparent in Vs structure (Figure 4d), but the amplitudes of low-Vs bands off axis are generally lower than those for Vp, and as for Vp, the amplitude decreases with depth so the bands disappear at $> 1.4 \text{-km}$ depth (Figures 4e and 4f). At the segment center,

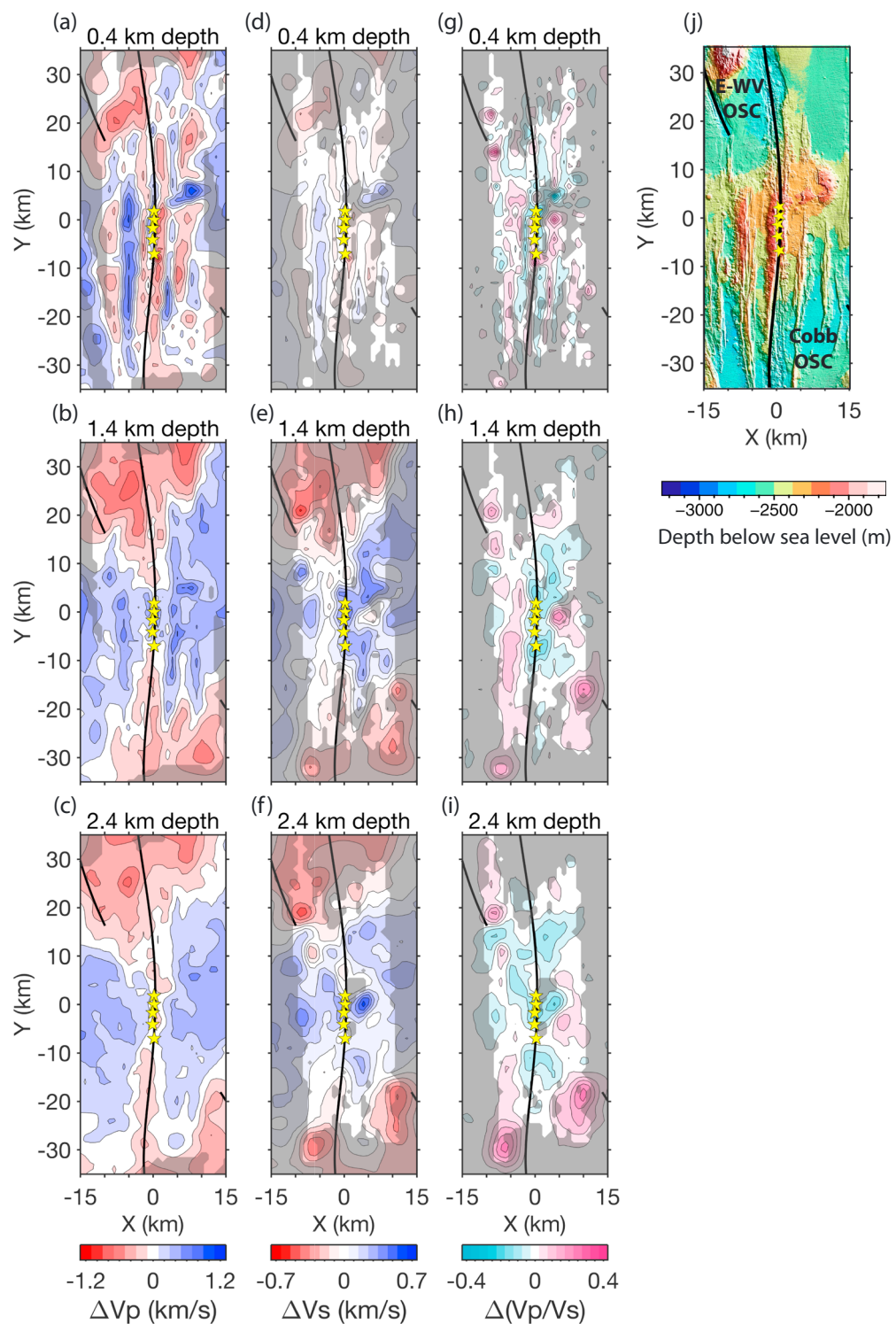


Figure 4. Map view sections of velocity perturbations to the horizontally averaged model. (a–c) V_p , (d–f) V_s , and (g–i) V_p/V_s anomalies at 0.4-, 1.4-, and 2.4-km depth are plotted in the area shown as a blue-dashed box in Figure 1a. Poorly resolved regions where the derivative weight sum is less than 10 are masked (Figure S2); the V_s mask is also used for V_p/V_s . The contour intervals for V_p , V_s , and V_p/V_s perturbations are 0.2 km/s, 0.1 km/s, and 0.05, respectively. Hydrothermal vent fields and the traces of the segments are shown as yellow stars and bold black lines, respectively. (j) Bathymetric map of the area shown in the other panels with labels of the E-WV and Cobb OSCs.

two regions of high V_p/V_s are observed at 1.4-km depth (Figure 4h): a band to the west of the axis that is ~4 km wide and extends ~30 km to the south and a circular region to the east of the segment center.

Figure 5 compares the vertical variations of average V_p , V_s , and V_p/V_s for several contrasting areas. At the segment center, V_p at depths ≥ 0.6 km is substantially higher on the flanks than near the segment center, whereas average V_s is only slightly higher off axis, so that V_p/V_s is markedly lower on axis. For example, at 1.4-km depth V_p/V_s is 1.72 on axis but little changed from the starting value of 1.8 on the west flank (Figure 5e). In the OSCs, both V_p and V_s are lower, but the fractional change in V_s is higher and becomes more so with increasing depth, leading to a high V_p/V_s that increases with depth. For example, in the Cobb OSC V_p/V_s increases from 1.82 at 0.6-km depth to 1.9 at 2.4-km depth (Figure 5e).

The differences between on- and off-axis structures near the center of the segment are well illustrated in vertical cross sections oriented perpendicular to the spreading axis through the Salty Dawg and High Rise vent fields (Figure 6). At depths between 1 and 2 km, V_s is high beneath the hydrothermal vent fields and relatively low in two regions 4 and 6 km to the west and east of the axis, respectively (Figures 6b and 6e). In contrast, V_p is generally high off axis and low- V_p anomalies are not observed ~5 km off axis (Figures 6a and 6d). As a result, V_p/V_s is low beneath the vent fields and high on the flanks.

Vertical cross sections oriented along the ridge axis show that at depths ≤ 2 km V_p and V_s beneath the hydrothermal vent fields are generally higher than to the north and south (Figures 7a and 7b). From 0.6- to 2.0-km depth, average V_p and V_s along the ridge axis are ~5.5 and ~3.0 km/s, respectively, and increase beneath the vent files by ~0.2 and ~0.3 km/s. Thus, beneath the vent fields V_s increases by ~10% while V_p increases by only ~4% and so V_p/V_s decreases by ~6%. The V_s model shows three regions of particular high-velocity anomalies beneath the Mothra vent field, between the High Rise and Salty Dawg fields, and beneath and to the north of the Sasquatch field (Figure 7b), and since variations in V_p are more muted (Figure 7a), three low- V_p/V_s anomalies are observed at the same locations (Figure 7c).

5. Discussion

We have presented a three-dimensional inversion for both V_p and V_s in the upper crust at the Endeavour segment of the JdFR, the first such inversion obtained at a mid-ocean ridge. The inversion includes a coupling constraint between V_p and V_s to ensure that lateral variations in V_p/V_s are required by the data. In this discussion, we first briefly compare our model with an earlier study of the one-dimensional V_p and V_s structure at the Endeavour segment and then interpret our three-dimensional V_p , V_s , and V_p/V_s model in terms of the effects of seafloor spreading, hydrothermal circulation, and regional tectonics on the distribution and aspect ratio of cracks in the shallow crust.

5.1. Comparison With an Earlier 1-D Inversion Model

The discrepancies between our results and an earlier one-dimensional inversion of Barclay and Wilcock (2004) can be explained by the limitations of this earlier study. Barclay and Wilcock (2004) jointly inverted microearthquake and explosive shot data from the ridge axis and west flank of Endeavour segment (Barclay & Wilcock, 2004) and found that V_p/V_s ratios are 2.75–2.90 above 0.25 km and 1.8–1.9 below 0.5-km depth. Their V_p/V_s for layer 2B in both on- and off-axis regions are generally higher than our results on the central axis and the west flank (Figure 5e). At depths ≤ 1.6 km they found in agreement with our results that V_p/V_s is higher off axis than on axis, but at greater depths V_p/V_s decreases substantially in their off-axis model. The discrepancies between our model and this earlier study likely reflect differences in the starting model (Barclay and Wilcock, 2004, have lower V_p/V_s in layer 2A) and the inherent trade-offs between earthquake focal depths and velocity structures in the one-dimensional joint inversions of earthquakes and shot data (Barclay & Wilcock, 2004). In their study, V_p is unconstrained by the explosive shot traveltimes below 1.5- to 2-km depth with no independent constraints on the V_s structure (Barclay & Wilcock, 2004). Most of the axial earthquakes were located between 2- and 3-km depths (Wilcock et al., 2002). Somewhat counterintuitively, Barclay and Wilcock (2004) found that when earthquakes are forced to shallower depths, both V_p and V_s increase and V_p/V_s decreases, changes that would make their results more similar to ours.

5.2. Lateral Heterogeneity of V_p/V_s Ratios and Cracks

Weekly et al. (2014) interpreted low V_p in the upper crust in and adjacent to the OSCs at both ends of the Endeavour segment (Figures 4a–4c) as evidence of a crust that had undergone pervasive tectonic

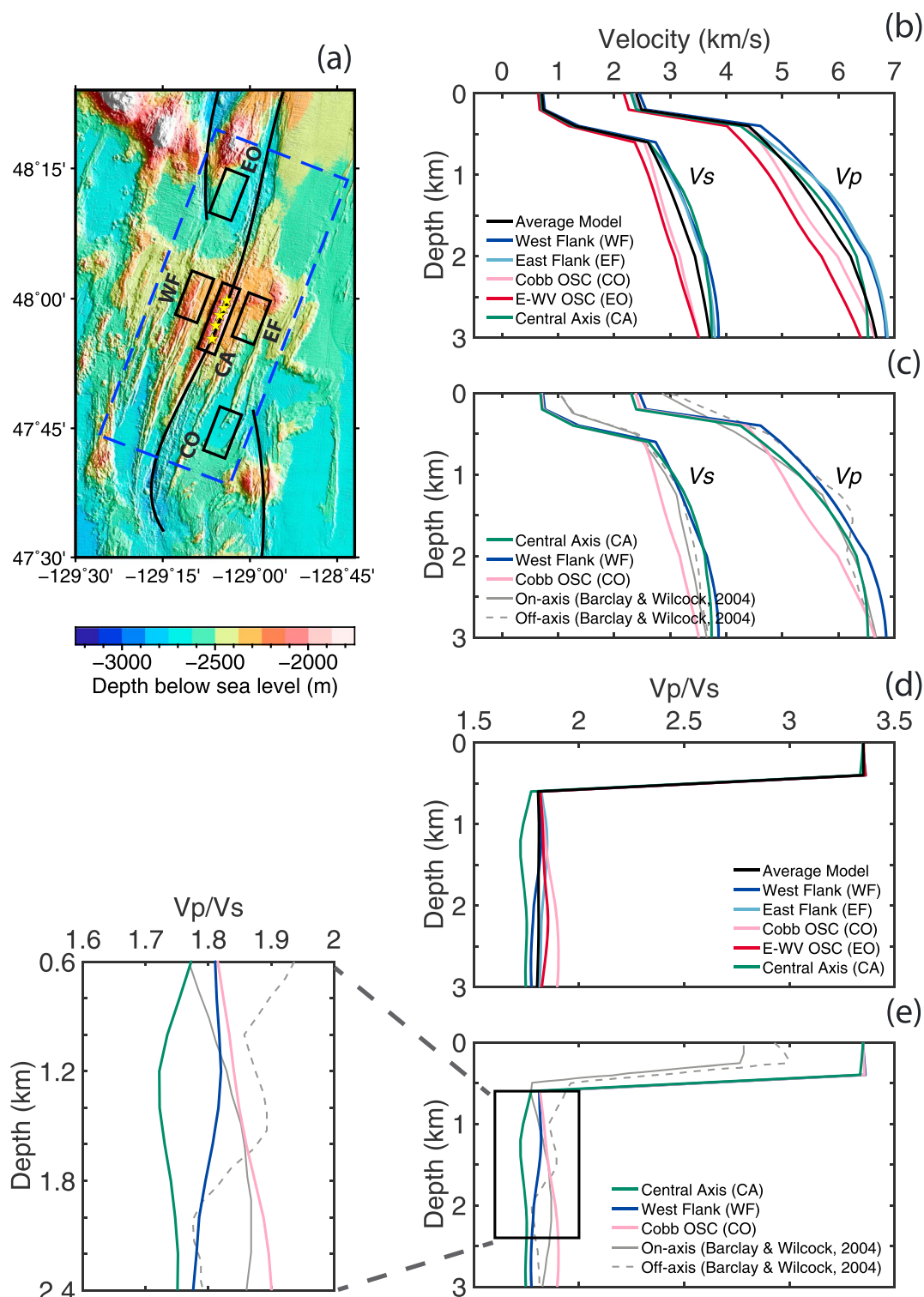


Figure 5. The horizontally averaged velocity profiles. (a) Bathymetric map showing labeled locations of five regions (black rectangles) used to derive the vertical profiles of averaged velocity; WF = west flank; EF = east flank; CO = Cobb OSC; EO = E-WV OSC; CA = central axis. (b) The depth profiles of V_p and V_s for the WF, EF, CO, EO, and CA regions are shown as colored lines and that of the average model in an area (dashed blue box) including the crustal grid as a black line. (c) V_p and V_s profiles for the CA, WF, and CO regions are compared with the profiles previously obtained for on- and off-axis regions (solid and dashed gray lines, respectively) at the Endeavour segment by Barclay and Wilcock (2004). (d) The depth profiles of V_p/V_s for the average model and the WF, EF, CO, EO, and CA regions are plotted with the same color conventions as in Figure 5b. (e) V_p/V_s profiles for the CA, WF, and CO regions are compared with the on- and off-axis profiles of Barclay and Wilcock (2004).

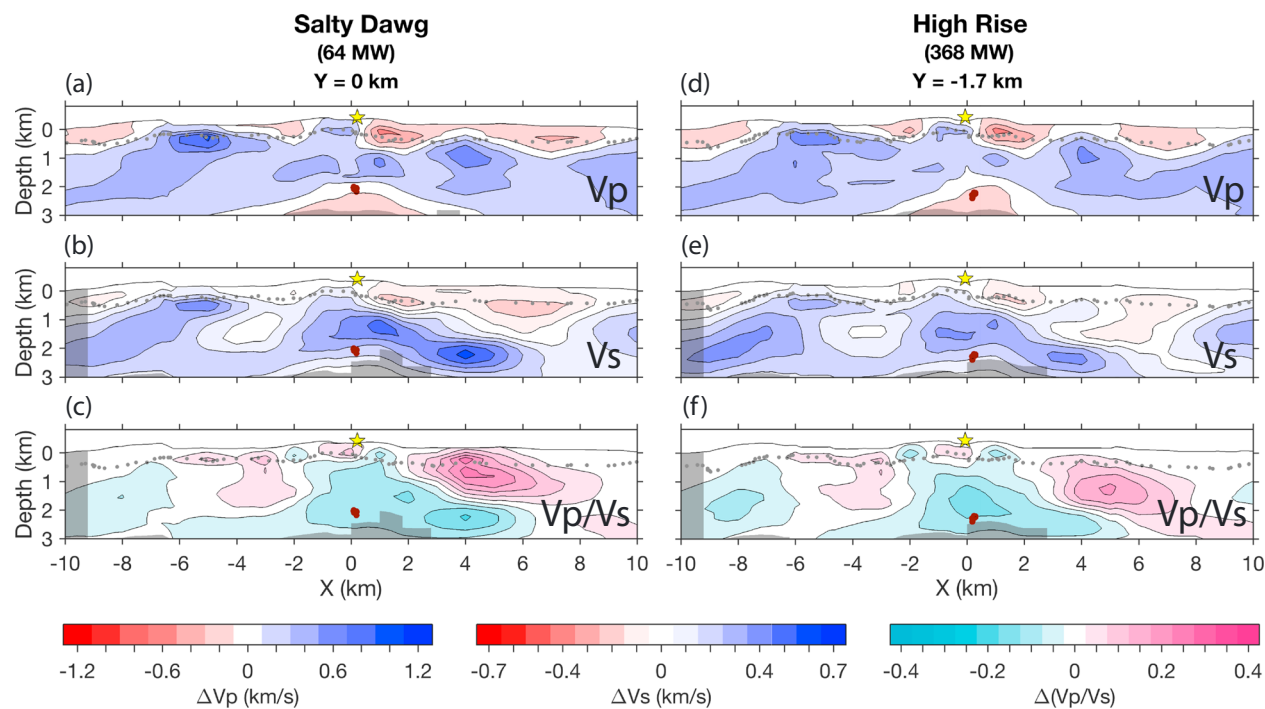


Figure 6. Across-axis vertical sections of velocity perturbations to the horizontally averaged model. V_p , V_s , and V_p/V_s anomalies beneath (a–c) the Salty Dawg and (d–f) the High Rise vent field (yellow star), labeled with the heat flux (Kellogg, 2011) and a location on the Y axis, are plotted. The bottom of layer 2A (gray dots; Van Ark et al., 2007) and the top boundary of the axial magma chamber (dark brown dots) are also shown.

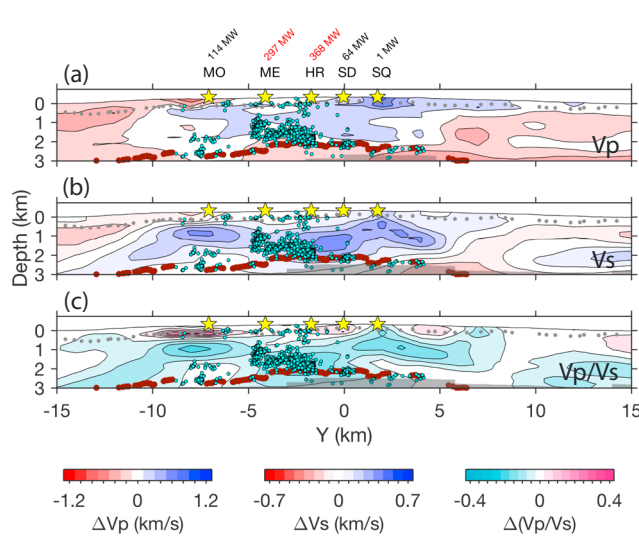


Figure 7. Along-axis vertical sections of velocity perturbations to the horizontally averaged model. (a) V_p , (b) V_s , and (c) V_p/V_s anomalies beneath the hydrothermal vent fields (yellow stars), labeled with the field names (MO = Mothra; ME = Main Endeavour; HR = High Rise; SD = Salty Dawg; SQ = Sasquatch) and the heat fluxes (Kellogg, 2011), are plotted.

Hypocenters for earthquakes recorded between 2003 and 2004 (cyan circles; Wilcock et al., 2009), the bottom of layer 2A (gray dots; Van Ark et al., 2007), and the top boundary of the axial magma chamber (dark brown dots; Van Ark et al., 2007) are also shown.

fracturing that recorded the history of ridge propagation. S wave velocities are not resolved over as large an area as V_p at the segment ends (Figure S2), but V_s is also low in this region (Figures 4d–4f) and the fractional velocity anomalies are larger for V_s so that V_p/V_s anomalies are positive (Figures 4g–4i). Based on our DEM models (Figure 3c), the high V_p/V_s requires thin cracks with aspect ratios <0.02 . This is consistent with a broad region of shear deformation within and adjacent to the large OSCs that forms narrow mode II cracks.

A remarkable feature of velocity structure in layer 2B in the central portion of the segment are the across-axis variations in V_p , V_s , and V_p/V_s (Figure 8). At 1.4-km depth, average isotropic V_p within 5–10 km of the ridge axis (crustal ages of 0.2–0.4 Ma) increases by ~0.4 km/s compared to the value at the ridge axis (Figure 8a). This increase in V_p is accompanied by a decrease in P wave anisotropy (Weekly et al., 2014) to a level that is less than half of the value at the ridge axis (Figure 8a). This decrease in anisotropy with distance from the ridge is attributed to infilling of cracks by mineral precipitation in the near-axis hydrothermal system (Weekly et al., 2014). The average V_s also generally increases off axis, but the minimum V_s is offset 3 km to the west of the ridge axis and V_s increases by less to the west than to the east (Figure 8b). The average V_p/V_s has a minimum of ~1.75 on and just to the east of the ridge axis and increases significantly on both flanks to maximum values of 1.83 at 10 km off axis to the east and 1.85 at 5 km off axis to the west (Figure 8c).

5.3. Across-Axis Model of Crack Distribution Within Layer 2B

We infer that the observed variation in V_p/V_s is primarily related to changes in the density and geometry of cracks. The effect of

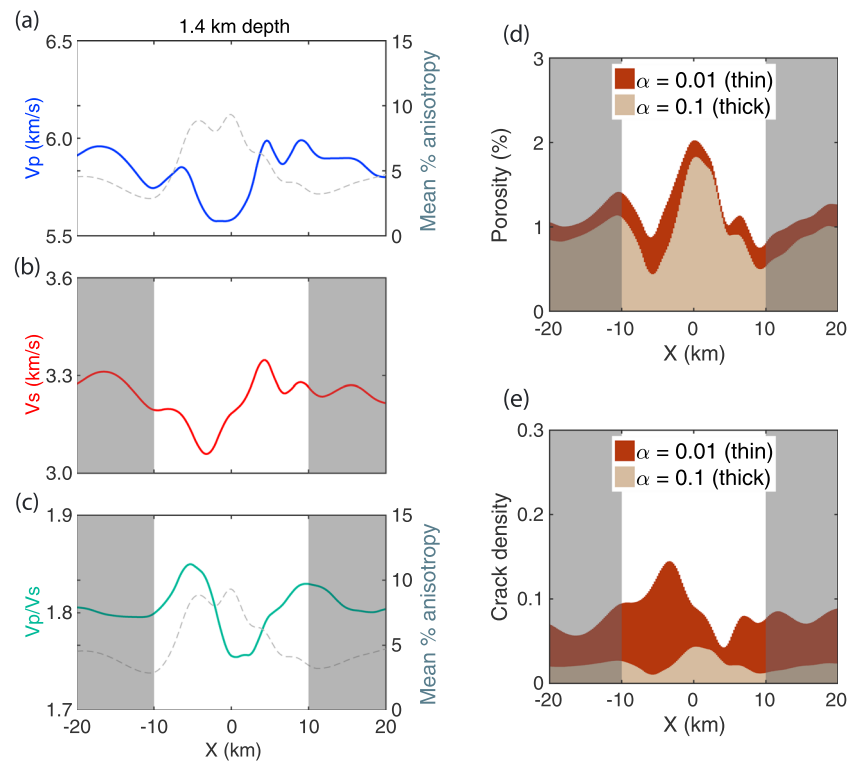


Figure 8. Average velocities, porosity, and crack density at 1.4-km depth as a function of distance from the ridge axis of the central part of the Endeavour segment. (a) V_p , (b) V_s , and (c) V_p/V_s averages over 2-km-wide bins extending 40 km along axis. The magnitude of the P wave anisotropy reported by Weekly et al. (2014) is overlaid on Figures 8a and 8c. The distributions of (d) porosity and (e) crack density calculated from the V_p and V_s averages are stacked to show the contribution from thick (crack aspect ratio = 0.1, light brown color) and thin (aspect ratio = 0.01, brown color) cracks to the total (see text). Gray shading indicates regions where V_s is not resolved.

temperature is likely to be very small at 1.4-km depth. Christensen (1996) shows that the Poisson's ratio of rocks does not vary significantly from 0 to 700 °C at 600 MPa. These results are supported by subsequent sample studies by Kern et al. (2001). In addition, we do not think that melt is a plausible source of the V_p/V_s variations at a depth of 1.4 km (layer 2B). Finally, while composition affects V_p/V_s , the range of Poisson's ratio observed in the upper oceanic crust by us and previous authors (e.g., Carlson, 2014b; Spudich & Orcutt, 1980) is too large to be explained by reasonable compositional variations. Thus, V_p/V_s variations in the upper oceanic crust are primarily related to its porosity and fracture characteristics.

We use our DEM results to construct a simple model to understand the relationship between V_p/V_s and the density and geometry of cracks. At 1.4-km depth, the observed V_p and V_s have the range of 5.5–6.2 and 3.0–3.4 km/s, respectively, and in these ranges the predicted V_p and V_s decrease approximately linearly with increasing porosity (Figures 3a and 3b) and so we can calculate the derivatives of V_p and V_s with porosity ($\partial V_p / \partial \phi$ and $\partial V_s / \partial \phi$) for each crack aspect ratio. The DEM theory assumes that only one crack aspect ratio is present, but we make the assumption that in the region of linear changes of velocity with porosity, the effects of cracks of different aspect ratio can be combined linearly. We combine DEM models with thin ($\alpha = 0.01$) and thick ($\alpha = 0.1$) cracks and write the velocities as follows:

$$V_p = V_{P,\phi=0} + \phi_{\alpha=0.01} \left(\frac{\partial V_p}{\partial \phi} \right)_{\alpha=0.01} + \phi_{\alpha=0.1} \left(\frac{\partial V_p}{\partial \phi} \right)_{\alpha=0.1} \quad (10)$$

$$V_s = V_{S,\phi=0} + \phi_{\alpha=0.01} \left(\frac{\partial V_s}{\partial \phi} \right)_{\alpha=0.01} + \phi_{\alpha=0.1} \left(\frac{\partial V_s}{\partial \phi} \right)_{\alpha=0.1} \quad (11)$$

$$\begin{bmatrix} \left(\frac{\partial V_p}{\partial \phi} \right)_{a=0.01} & \left(\frac{\partial V_p}{\partial \phi} \right)_{a=0.1} \\ \left(\frac{\partial V_s}{\partial \phi} \right)_{a=0.01} & \left(\frac{\partial V_s}{\partial \phi} \right)_{a=0.1} \end{bmatrix} = \begin{bmatrix} -0.95 & -0.35 \\ -0.69 & -0.10 \end{bmatrix}. \quad (12)$$

For each average V_p and V_s value in the across-axis profiles of Figures 8a and 8b, we solve equations (10) and (11) for the porosity due to thin ($\phi_a = 0.01$) and thick ($\phi_a = 0.1$) cracks (Figure 8d). We also express our solutions in terms of the crack density ϵ (Figure 8e), which is defined as $\epsilon = Na^3/V$, where N is the number of cracks per volume V and a is the crack radius. For ellipsoidal cracks, porosity is related to ϵ by $\phi = \frac{4}{3}\pi a \epsilon$, where a is the crack aspect ratio (Le Ravalec & Guéguen, 1996; Mavko et al., 2009; Shearer, 1988).

The results suggest that the porosity is everywhere dominated by thick cracks and that the highest porosities and densities of thick cracks are found near the ridge axis. Within 3 km of the ridge, the average total porosity is 1.82% and is formed from a porosity of 1.57% and 0.25% from thick and thin cracks, respectively. In contrast, at distances of 5–10 km off axis the average porosities are 0.95–1.11% and are formed from porosities of 0.72–0.75% and 0.23–0.36% from thick and thin cracks, respectively (Figure 8d).

5.4. Crack Geometry and Seafloor Spreading, Hydrothermal Circulation, and Tectonics

Previous studies of the P wave velocities in the uppermost portion of layer 2B from multichannel seismic profiles (Newman et al., 2011) and of P wave velocities and anisotropy from the tomography data set used in our study (Weekly et al., 2014) show that V_p in layer 2B increases markedly within ~5 km of the ridge axis with anisotropy decreasing over similar distances. This was interpreted as evidence of the rapid infilling of cracks in the near axis hydrothermal system. Our results suggest that this change in seismic velocity and anisotropy is accomplished by a substantial reduction in the density of thicker cracks (Figure 8e).

Wilkins et al. (1991) modeled the rapid V_p increase in the layer 2A of the oceanic crust by invoking the sealing of only thin cracks (low aspect ratio pores). They assumed that closing of thin cracks controlled V_p variations arguing that V_p is very sensitive to small aspect ratio cracks and that it is harder to close thick cracks by hydrothermal precipitation. This is a reasonable inference in a region dominated by pillow lavas where each fluid pathway alternates between relatively thin cracks separating touching pillows and larger voids where several pillows meet. In contrast, our V_p/V_s results show that in layer 2B thick cracks are more susceptible to closure. This may be because in a layer where the porosity is dominated by vertical cracks, the thicker cracks support higher hydrothermal precipitation rates as a consequence of a higher fluid flux that is proportional to the cube of a conduit radius and because the thick cracks are also better connected to the permeable network.

We infer that the high density of thick cracks near the ridge axis is indicative of a region where cracks are opening as a result of extensional strains due to plate spreading. Along fast and intermediate spreading rate ridges, oceanic crust is produced in a volcanic zone that is 1–2 km wide and is subsequently fissured and tectonically deformed by normal faults within 2–3 km of the ridge axis (Macdonald, 1982). Studies of fault distributions on the EPR show that near the axis, there are many wide, vertical fissures (Mode I: opening mode) created by fast extension cracking and related to magma inflation and hydrothermal cooling (Wright, 1998). In contrast, faults are narrower off axis than on axis because they are created by shear failure (Mode II: sliding mode) in which the material on one side of the cracks is sliding past the other rather than pulling apart (Wright, 1998). At the Endeavour, the axial valley and its walls are highly tectonized with many prominent ridge-parallel fissures and faults (Delaney et al., 1992; Glickson et al., 2007). Hydrothermal modeling studies also require that layer 2B permeability is several orders of magnitude higher on axis than off axis (e.g., Lowell & Germanovich, 2004), a result that suggests cracks at depth on axis are thicker. Microearthquake studies show that the rates of seismicity are high above the AMC owing to cracking caused by a combination of plate extension, hydrothermal cooling (Wilcock et al., 2002), and magma inflation (Wilcock et al., 2009), all of which may open wide cracks if the failure mode includes a Mode I extensional component.

We infer that as the crust moves out of the zone of active extension, hydrothermal fluids, which preferentially circulate through thick cracks, fill these cracks with precipitates and alteration minerals (Turcotte & Schubert, 2014; Wilcock & Delaney, 1996), and so that in the absence of continued extension the cracks narrow and circulation becomes less vigorous. This is consistent with a model in which vigorous hydrothermal

circulation near the ridge axis (<5 km) extracts a large amount of heat from the crust, resulting in a reduced geothermal gradient within the cooled region, and conductive heat flow becomes a primary mechanism of vertical heat transport on the ridge flanks (Cochran & Buck, 2001). In addition, Hasenclever et al. (2014) showed the 2-D model of a combination of crustal accretion and hydrothermal flow in which a decrease in permeability beyond a distance of 5 km from the ridge axis indicates colder and broader recharge up to several kilometers away from the axis that feeds hot (500–700 °C) deep-rooted off-axis flow toward the ridge.

The predicted across-axis distribution of thin cracks from our model is more complex than for thick cracks (Figures 8d and 8e). Rather than showing a decrease in density moving off axis, the distribution of thin cracks is very asymmetric with a minimum density 4 km off axis to the east and a maximum density 4 km off axis to the west. This complexity may in part reflect the simplicity of our model, which assumes all the cracks have aspect ratios of either 0.1 or 0.01 and which ignores the effects of variations in composition, hydrothermal alteration, and thermal structure. However, two first-order characteristics of the distribution do require explanation.

First, the lack of a clear decrease in thin crack density well off axis suggests that there is a significant population of thin cracks whose density does not change systematically within 10 km (~0.4 Ma) of the ridge axis. Thin cracks are only a minor contribution to the total porosity, but they have a higher density than the thick cracks. Either these thin cracks are backwaters through which hydrothermal fluids do not circulate or the hydrothermal flow velocities and rates of alteration and precipitation in these cracks are very low. Newman et al. (2011) found that V_p in layer 2B does not change appreciably at ages >0.5 Ma out to the maximum ages sampled (3.5 Ma at the Endeavour and 7 Ma elsewhere on the JdFR) so we infer that to the extent that thin cracks in layer 2B off axis are filled by hydrothermal alteration products, they are regenerated by off-axis normal faulting.

Second, the lower V_s and higher V_p/V_s on the west flank suggest a higher density of thin cracks in this region. This inference is supported by asymmetry in the P wave anisotropy. Anisotropy decreases rapidly off axis on the east flank but remains high out to ~5 km where the density of thin cracks reaches its maximum value. There must be some mechanism to produce more thin cracks on the west flank, and we speculate that they are related to internal deformation of the Pacific plate. Wilcock et al. (2002) recorded a large number of midcrustal microearthquakes out to 15 km off axis on the Pacific plate with strike-slip mechanisms indicative of north-south compression which were interpreted either as evidence that the west flank of the Endeavour was deforming in response to the breakup of the Explorer microplate (Kreemer et al., 1998) or that it is now part of the Sovanco transform deformation zone. Based on detailed regional bathymetric mapping and the distribution of hydroacoustically detected earthquakes, Dziak (2006) argues that the shear zone separating the Pacific and Explorer plates extends well south of the Sovanco Fracture Zone to include the Heck and Hecke seamounts on the west flank of the Endeavour, and potentially as far south as the Springfield Seamounts and Cobb OSC.

5.5. Evolution of Crack Distributions and Hydrothermal Circulation

Arnoux et al. (2017) used full waveform inversions to obtain a high resolution V_p model in the upper crust on the central portion of the Endeavour. They interpreted variations in V_p immediately above the AMC in terms of variations in crack density and by implication permeability. The two fields with the highest heat fluxes, the Main Endeavour and High Rise fields, are underlain by the lowest V_p and high rates of seismicity immediately above the AMC, consistent with the view that ongoing fracturing due to magma chamber inflation maintains the high permeability necessary to support high hydrothermal fluxes (Wilcock et al., 2009). In contrast, V_p is highest above the AMC beneath the Salty Dawg and Sasquatch fields that have the lowest heat fluxes, low rates of seismicity, and by inference low permeabilities. The resolution of V_s model is insufficient to fully resolve differences on the 2-km scale of the vent field spacing (Figures S3 and S4), but it does show that V_s is generally low beneath the hydrothermal vent fields compared with the ridge axis immediately to the north and south (Figure 7b). The V_p/V_s ratio is low everywhere beneath the vent fields from 0.5- to 2-km depth (Figure 7c) consistent with the idea discussed above that the cracks tend to be wider in the extensional environment of the ridge axis.

Figure 9 is a cartoon which summarizes our model for the evolution of crack distributions. Newman et al. (2011) suggested that layer 2B evolution is strongly affected by mineral precipitation due to active

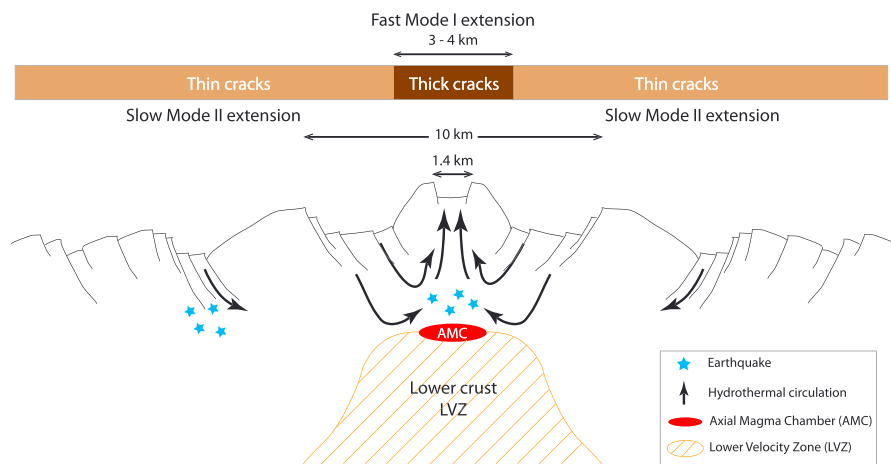


Figure 9. Conceptual illustration for crack generation and hydrothermal circulation in on- and off-axis regions at the Endeavour segment. Beneath the ridge axis, extension due to spreading results in wide vertical fissures (thick cracks) that provide long-term conduits for upflow in high-temperature hydrothermal vent fields supported by heat source from the axial magma chamber (Van Ark et al., 2007). On the ridge flanks, narrow faults (thin cracks) created by normal faulting provide pathways for hydrothermal downflow. On-axis earthquakes result from plate spreading, magma inflation, and hydrothermal cooling, while off-axis earthquakes on the west flank result from the internal deformation of the Pacific plate.

hydrothermal circulation and that reduced and increased V_p in the upper layer 2B mark the locations of hydrothermal discharge (upflow) and recharge (downflow) zones, respectively. Thus, the low V_p in layer 2B within 0–2 km of the ridge axis and high V_p within 5–10 km correspond to upflow and downflow zones of hydrothermal circulation, respectively (Figure 9). This is consistent with the fluid circulation model, inferred from the heat flow measurements, in which seawater enters in the Endeavour ridge flanks and fluid is upwelling at the ridge axis (Johnson et al., 1993). Arnoux et al. (2017) used a high-resolution 3-D V_p structure to interpret low V_p anomalies within 1–2 km of the ridge axis as normal faults that provide pathways for hydrothermal recharge. Our V_p/V_s results suggest that in fact, faulting out to ~5 km from the ridge contributes pathways for hydrothermal downflow. We infer that low V_p/V_s beneath the ridge axis indicates the dominance of thick cracks in the upflow zone, whereas high V_p/V_s in the flanks indicates large numbers of thin cracks in a region that contributes to downflow (Figure 9). Since a fissure, defined as an open, Mode I tension crack initiating at the surface, provides an important conduit for upward fluids (Wright, 1998), the large proportion of thick cracks at the ridge axis may contribute to the development of high-temperature hydrothermal vent fields (e.g., Glickson et al., 2007). When intrusions and eruptions cease as the crust moves off axis, crustal cooling and slow extension by normal faulting continue to produce thin Mode II cracks at a rate that is sufficient to support a broad region of hydrothermal recharge. In addition, the internal deformation of the Pacific Plate leads to a higher density of think cracks on the west flank.

6. Conclusions

We present a joint inversion for three-dimensional V_p and V_s structures in the upper crust of the Endeavour segment that includes coupling constraints between V_p and V_s . The DEM theory is used to predict V_p and V_s as a function of porosity and crack aspect ratio. The results indicate that the heterogeneous V_p/V_s in layer 2B is related to the variations in the proportions of thin and thick cracks. Low V_p and V_s and a decrease in V_p/V_s within a few kilometers of the ridge axis is attributed to the increased density of thick cracks that provides the conduits to maintain high permeability in the upflow zone of hydrothermal circulation. We infer that hydrothermal alteration products fill these cracks once they move outside the region of ridge extension leading to higher V_p/V_s on the ridge flanks. Low V_p and V_s and high V_p/V_s in the OSCs are consistent with a high density of thin cracks produced by shear deformation.

Acknowledgments

We thank the officers and crew of the R/V *Marcus G. Langseth* as well as the OBS teams from Scripps Institution of Oceanography and Woods Hole Oceanographic Institution for their assistance in the acquisition of the seismic data. Additional assistance was provided by onboard passive acoustic technicians and marine mammal observers to ensure that data collection was accomplished in compliance with guidelines set forth by marine environmental assessments and permits. We thank David Mainprice for his constructive comments on the DEM modeling. We also thank the Editor Maureen Long, Gail Christeson, and an anonymous reviewer for their insightful and thoughtful comments to improve this manuscript. This work was supported by Creative-Pioneering Researchers Program through Seoul National University (SNU SRND 3345-20160014) and by the Nuclear Safety Research Program through the Korea Foundation Of Nuclear Safety (KoFONS) using the financial resource granted by the Nuclear Safety and Security Commission (NSSC) of the Republic of Korea (1705010). The data collection was supported by NSF grants OCE-0454747 to the University of Oregon and OCE-0454700 to the University of Washington. The authors declare no competing interests. Raw seismic data from ETOMO are available at Data Management Center of Incorporated Research Institutions for Seismology (<http://obsip.iris.edu/experiments/experiment-table/2009/endeavor>). The 3-D velocity model is available in the Marine Geoscience Data System (<http://www.marine-geo.org/index.php>).

References

- Almendros, J., Barclay, A. H., Wilcock, W. S. D., & Purdy, G. M. (2000). Seismic anisotropy of the shallow crust at the Juan de Fuca Ridge. *Geophysical Research Letters*, 27(19), 3109–3112. <https://doi.org/10.1029/2000GL011535>
- Anderson, O. L., & Isaak, D. G. (1995). Elastic constants of mantle minerals at high temperature. In *Mineral physics & crystallography: A handbook of physical constants* (pp. 64–97). Washington, DC: American Geophysical Union.
- Arnoux, G. M., Toomey, D. R., Hooft, E. E. E., Wilcock, W. S. D., Morgan, J., Warner, M., & VanderBeek, B. P. (2017). Seismic evidence that black smoker heat flux is influenced by localized magma replenishment and associated increases in crustal permeability. *Geophysical Research Letters*, 44, 1687–1695. <https://doi.org/10.1029/2016GL071990>
- Arnulf, A. F., Harding, A. J., Singh, S. C., Kent, G. M., & Crawford, W. (2012). Fine-scale velocity structure of upper oceanic crust from full waveform inversion of downward continued seismic reflection data at the Lucky Strike Volcano, Mid-Atlantic Ridge. *Geophysical Research Letters*, 39, L08303. <https://doi.org/10.1029/2012GL051064>
- Au, D., & Clowes, R. M. (1984). Shear-wave velocity structure of the oceanic lithosphere from ocean bottom seismometer studies. *Geophysical Journal International*, 77(1), 105–123. <https://doi.org/10.1111/j.1365-246X.1984.tb01927.x>
- Barclay, A. H., & Toomey, D. R. (2003). Shear wave splitting and crustal anisotropy at the Mid-Atlantic Ridge, 35°N. *Journal of Geophysical Research*, 108(B8), 2378. <https://doi.org/10.1029/2001JB000918>
- Barclay, A. H., Toomey, D. R., & Solomon, S. C. (1998). Seismic structure and crustal magmatism at the Mid-Atlantic Ridge, 35°N. *Journal of Geophysical Research*, 103(B8), 17,827–17,844. <https://doi.org/10.1029/98JB01275>
- Barclay, A. H., Toomey, D. R., & Solomon, S. C. (2001). Microearthquake characteristics and crustal V_p/V_s structure at the Mid-Atlantic Ridge, 35°N. *Journal of Geophysical Research*, 106(B2), 2017–2034. <https://doi.org/10.1029/2000JB900371>
- Barclay, A. H., & Wilcock, W. S. D. (2004). Upper crustal seismic velocity structure and microearthquake depths at the Endeavour segment, Juan de Fuca Ridge. *Geochemistry, Geophysics, Geosystems*, 5, Q01004. <https://doi.org/10.1029/2003GC000604>
- Bazin, S., Harding, A. J., Kent, G. M., Orcutt, J. A., Singh, S. C., Tong, C. H., et al. (2003). A three-dimensional study of a crustal low velocity region beneath the 9°03'N overlapping spreading center. *Geophysical Research Letters*, 30(2), 1039. <https://doi.org/10.1029/2002GL015137>
- Berge, P. A., Berryman, J. G., & Bonner, B. P. (1993). Influence of microstructure on rock elastic properties. *Geophysical Research Letters*, 20(23), 2619–2622. <https://doi.org/10.1029/93GL03131>
- Berge, P. A., Fryer, G. J., & Wilkens, R. H. (1992). Velocity-porosity relationships in the upper oceanic crust: Theoretical considerations. *Journal of Geophysical Research*, 97(B11), 15,239–15,254. <https://doi.org/10.1029/92JB01464>
- Bratt, S. R., & Solomon, S. C. (1984). Compressional and shear wave structure of the East Pacific Rise at 11°20'N: Constraints from three-component ocean bottom seismometer data. *Journal of Geophysical Research*, 89(B7), 6095–6110. <https://doi.org/10.1029/JB089iB07p06095>
- Brocher, T. M. (2005). Empirical relations between elastic wavespeeds and density in the Earth's crust. *Bulletin of the Seismological Society of America*, 95(6), 2081–2092. <https://doi.org/10.1785/0120050077>
- Bruner, W. M. (1976). Comment on 'Seismic velocities in dry and saturated cracked solids' by Richard J. O'Connell and Bernard Budiansky. *Journal of Geophysical Research*, 81(14), 2573–2576. <https://doi.org/10.1029/JB081i014p02573>
- Budiansky, B. (1965). On the elastic moduli of some heterogeneous materials. *Journal of the Mechanics and Physics of Solids*, 13(4), 223–227. [https://doi.org/10.1016/0022-5096\(65\)90011-6](https://doi.org/10.1016/0022-5096(65)90011-6)
- Canales, J. P., Detrick, R. S., Toomey, D. R., & Wilcock, W. S. D. (2003). Segment-scale variations in the crustal structure of 150–300 kyr old fast spreading oceanic crust (East Pacific Rise, 8°15'N–10°5'N) from wide-angle seismic refraction profiles. *Geophysical Journal International*, 152(3), 766–794. <https://doi.org/10.1046/j.1365-246X.2003.01885.x>
- Carlson, R. L. (2010). How crack porosity and shape control seismic velocities in the upper oceanic crust: Modeling downhole logs from Holes 504B and 1256D. *Geochemistry, Geophysics, Geosystems*, 11, Q04007. <https://doi.org/10.1029/2009GC002955>
- Carlson, R. L. (2014a). The influence of porosity and crack morphology on seismic velocity and permeability in the upper oceanic crust. *Geochemistry, Geophysics, Geosystems*, 15, 10–27. <https://doi.org/10.1029/2013GC004965>
- Carlson, R. L. (2014b). The effects of alteration and porosity on seismic velocities in oceanic basalts and diabases. *Geochemistry, Geophysics, Geosystems*, 15, 4589–4598. <https://doi.org/10.1029/2014GC005537>
- Cheung, H. P. Y., & Clowes, R. M. (1981). Crustal structure from P- and S-wave analyses: Ocean bottom seismometer results in the north-East Pacific. *Geophysical Journal International*, 65(1), 47–73. <https://doi.org/10.1111/j.1365-246X.1981.tb02700.x>
- Christensen, N. I. (1996). Poisson's ratio and crustal seismology. *Journal of Geophysical Research*, 101(B2), 3139–3156. <https://doi.org/10.1029/95JB03446>
- Christensen, N. I., & Mooney, W. D. (1995). Seismic velocity structure and composition of the continental crust: A global view. *Journal of Geophysical Research*, 100(B6), 9761–9788. <https://doi.org/10.1029/95JB00259>
- Christeson, G. L., Purdy, G. M., & Fryer, G. J. (1994). Seismic constraints on shallow crustal emplacement processes at the fast spreading East Pacific Rise. *Journal of Geophysical Research*, 99(B9), 17,957–17,973. <https://doi.org/10.1029/94JB01252>
- Christeson, G. L., Shaw, P. R., & Garmany, J. D. (1997). Shear and compressional wave structure of the East Pacific Rise, 9°–10°N. *Journal of Geophysical Research*, 102(B4), 7821–7835. <https://doi.org/10.1029/96JB03901>
- Cochran, J. R., & Buck, W. R. (2001). Near-axis subsidence rates, hydrothermal circulation, and thermal structure of mid-ocean ridge crests. *Journal of Geophysical Research*, 106(B9), 19,233–19,258. <https://doi.org/10.1029/2001JB000379>
- Collier, J. S., & Singh, S. C. (1998). Poisson's ratio structure of young oceanic crust. *Journal of Geophysical Research*, 103(B9), 20,981–20,996. <https://doi.org/10.1029/98JB01980>
- Crawford, W. C., Webb, S. C., & Hildebrand, J. A. (1999). Constraints on melt in the lower crust and Moho at the East Pacific Rise, 9°48'N, using seafloor compliance measurements. *Journal of Geophysical Research*, 104(B2), 2923–2939. <https://doi.org/10.1029/1998JB900087>
- Creager, K. C., & Dorman, L. M. (1982). Location of instruments on the seafloor by joint adjustment of instrument and ship positions. *Journal of Geophysical Research*, 87(B10), 8379–8388. <https://doi.org/10.1029/JB087iB10p08379>
- Delaney, J. R., Robigou, V., McDuff, R. E., & Tivey, M. K. (1992). Geology of a vigorous hydrothermal system on the Endeavour segment, Juan de Fuca Ridge. *Journal of Geophysical Research*, 97(B13), 19663. <https://doi.org/10.1029/92JB00174>
- DeMets, C., Gordon, R. G., & Argus, D. F. (2010). Geologically current plate motions. *Geophysical Journal International*, 181(1), 1–80. <https://doi.org/10.1111/j.1365-246X.2009.04491.X>
- Domenico, S. N. (1984). Rock lithology and porosity determination from shear and compressional wave velocity. *Geophysics*, 49(8), 1188–1195. <https://doi.org/10.1190/1.1441748>
- Dunn, R. A., & Toomey, D. R. (2001). Crack-induced seismic anisotropy in the oceanic crust across the East Pacific Rise (9°30'N). *Earth and Planetary Science Letters*, 189(1–2), 9–17. [https://doi.org/10.1016/S0012-821X\(01\)00353-3](https://doi.org/10.1016/S0012-821X(01)00353-3)

- Dziak, R. P. (2006). Explorer deformation zone: Evidence of a large shear zone and reorganization of the Pacific–Juan de Fuca–North American triple junction. *Geology*, 34(3), 213. <https://doi.org/10.1130/g22164.1>
- Eddy, D. R., Van Avendonk, H. J. A., & Shillington, D. J. (2013). Compressional and shear-wave velocity structure of the continent-ocean transition zone at the eastern Grand Banks, Newfoundland. *Geophysical Research Letters*, 40, 3014–3020. <https://doi.org/10.1002/grl.50511>
- Eshelby, J. D. (1957). The determination of the elastic field of an ellipsoidal inclusion, and related problems. *Proceedings of the Royal Society of London. Series A: Mathematical and Physical Sciences*, 241(1226), 376–396. <https://doi.org/10.2307/100095>
- Fowler, C. M. R. (1976). Crustal structure of the Mid-Atlantic Ridge crest at 37°N. *Geophysical Journal International*, 47(3), 459–491. <https://doi.org/10.1111/j.1365-246X.1976.tb07097.x>
- Glickson, D. A., Kelley, D. S., & Delaney, J. R. (2007). Geology and hydrothermal evolution of the Mothra hydrothermal field, Endeavour segment, Juan de Fuca Ridge. *Geochemistry, Geophysics, Geosystems*, 8, Q06010. <https://doi.org/10.1029/2007GC001588>
- Hammond, W. C., & Toomey, D. R. (2003). Seismic velocity anisotropy and heterogeneity beneath the Mantle Electromagnetic and Tomography Experiment (MELT) region of the East Pacific Rise from analysis of *P* and *S* body waves. *Journal of Geophysical Research*, 108(B4), 2176. <https://doi.org/10.1029/2002JB001789>
- Harding, A. J., Orcutt, J. A., Kappus, M. E., Vera, E. E., Mutter, J. C., Buhl, P., et al. (1989). Structure of young oceanic crust at 13°N on the East Pacific Rise from expanding spread profiles. *Journal of Geophysical Research*, 94(B9), 12163. <https://doi.org/10.1029/JB094iB09p12163>
- Hasenclever, J., Theissen-Krah, S., Rupke, L. H., Morgan, J. P., Iyer, K., Petersen, S., & Devey, C. W. (2014). Hybrid shallow on-axis and deep off-axis hydrothermal circulation at fast-spreading ridges. *Nature*, 508(7497), 508–512. <https://doi.org/10.1038/nature13174>
- Hill, R. (1965). A self-consistent mechanics of composite materials. *Journal of the Mechanics and Physics of Solids*, 13(4), 213–222. [https://doi.org/10.1016/0022-5096\(65\)90010-4](https://doi.org/10.1016/0022-5096(65)90010-4)
- Hooft, E. E. E., Detrick, R. S., Toomey, D. R., Collins, J. A., & Lin, J. (2000). Crustal thickness and structure along three contrasting spreading segments of the Mid-Atlantic Ridge, 33.5°–35°N. *Journal of Geophysical Research*, 105(B4), 8205–8226. <https://doi.org/10.1029/1999JB900442>
- Hooft, E. E. E., Patel, H., Wilcock, W., Becker, K., Butterfield, D., Davis, E., et al. (2010). A seismic swarm and regional hydrothermal and hydrologic perturbations: The northern Endeavour segment, February 2005. *Geochemistry, Geophysics, Geosystems*, 11, Q12015. <https://doi.org/10.1029/2010GC003264>
- Hornby, B. E., Schwartz, L. M., & Hudson, J. A. (1994). Anisotropic effective-medium modeling of the elastic properties of shales. *Geophysics*, 59(10), 1570–1583. <https://doi.org/10.1190/1.1443546>
- Hudson, J. A. (1980). Overall properties of a cracked solid. *Mathematical Proceedings of the Cambridge Philosophical Society*, 88(02), 371–384. <https://doi.org/10.1017/S0305000410005764>
- Hulme, T., Ricolleau, A., Bazin, S., Crawford, W. C., & Singh, S. C. (2003). Shear wave structure from joint analysis of seismic and seafloor compliance data. *Geophysical Journal International*, 155(2), 514–520. <https://doi.org/10.1046/j.1365-246X.2003.02061.x>
- Hung, S.-H., & Forsyth, D. W. (1999). Anisotropy in the oceanic lithosphere from the study of local intraplate earthquakes on the west flank of the southern East Pacific Rise: Shear wave splitting and waveform modeling. *Journal of Geophysical Research*, 104(B5), 10,695–10,717. <https://doi.org/10.1029/1999JB900046>
- Jacobson, R. S. (1992). Impact of crustal evolution on changes of the seismic properties of the uppermost ocean crust. *Reviews of Geophysics*, 30(1), 23–42. <https://doi.org/10.1029/91RG02811>
- Jakobsen, M., Hudson, J. A., Minshull, T. A., & Singh, S. C. (2000). Elastic properties of hydrate-bearing sediments using effective medium theory. *Journal of Geophysical Research*, 105(B1), 561–577. <https://doi.org/10.1029/1999JB900190>
- Johnson, H. P., Becker, K., & Von Herzen, R. (1993). Near-axis heat flow measurements on the northern Juan De Fuca Ridge: Implications for fluid circulation in oceanic crust. *Geophysical Research Letters*, 20(17), 1875–1878. <https://doi.org/10.1029/93GL00734>
- Johnston, J. E., & Christensen, N. I. (1997). Seismic properties of layer 2 basalts. *Geophysical Journal International*, 128(2), 285–300. <https://doi.org/10.1111/j.1365-246X.1997.tb01555.x>
- Kelley, D. S., Baross, J. A., & Delaney, J. R. (2002). Volcanoes, fluids, and life at mid-ocean ridge spreading centers. *Annual Review of Earth and Planetary Sciences*, 30(1), 385–491. <https://doi.org/10.1146/annurev.earth.30.091201.141331>
- Kelley, D. S., Delaney, J. R., & Yoerger, D. R. (2001). Geology and venting characteristics of the Mothra hydrothermal field, Endeavour segment, Juan de Fuca Ridge. *Geology*, 29(10), 959–962. [https://doi.org/10.1130/0091-7613\(2001\)029<0959:GAVCOT>2.0.CO;2](https://doi.org/10.1130/0091-7613(2001)029<0959:GAVCOT>2.0.CO;2)
- Kellogg, J. P. (2011). Temporal and spatial variability of hydrothermal fluxes within a mid-ocean ridge segment, (Doctoral dissertation). Seattle, WA: University of Washington.
- Kern, H., Popp, T., Gorbatsevich, F., Zharikov, A., Lobanov, K. V., & Smirnov, Y. P. (2001). Pressure and temperature dependence of *Vp* and *Vs* in rocks from the superdeep well and from surface analogues at Kola and the nature of velocity anisotropy. *Tectonophysics*, 338(2), 113–134. [https://doi.org/10.1016/S0040-1951\(01\)00128-7](https://doi.org/10.1016/S0040-1951(01)00128-7)
- Kreemer, C., Govers, R., Furlong, K. P., & Holt, W. E. (1998). Plate boundary deformation between the Pacific and North America in the Explorer region. *Tectonophysics*, 293(3), 225–238. [https://doi.org/10.1016/S0040-1951\(98\)00089-4](https://doi.org/10.1016/S0040-1951(98)00089-4)
- Le Ravalec, M., & Guégan, Y. (1996). High- and low-frequency elastic moduli for a saturated porous/cracked rock-differential self-consistent and poroelastic theories. *Geophysics*, 61(4), 1080–1094. <https://doi.org/10.1190/1.1444029>
- Lowell, R. P., & Germanovich, L. N. (2004). Hydrothermal Processes at Mid-Ocean Ridges: Results from Scale Analysis and Single-Pass Models. In C. R. German, J. Lin, & L. M. Parson (Eds.), *Mid-Ocean Ridges*. <https://doi.org/10.1029/148GM09>
- Macdonald, K. C. (1982). Mid-ocean ridges: Fine scale tectonic, volcanic and hydrothermal processes within the plate boundary zone. *Annual Review of Earth and Planetary Sciences*, 10(1), 155–190. <https://doi.org/10.1146/annurev.ea.10.050182.001103>
- Mainprice, D. (1997). Modelling the anisotropic seismic properties of partially molten rocks found at mid-ocean ridges. *Tectonophysics*, 279(1-4), 161–179. [https://doi.org/10.1016/S0040-1951\(97\)00122-4](https://doi.org/10.1016/S0040-1951(97)00122-4)
- Masters, G., Jordan, T. H., Silver, P. G., & Gilbert, F. (1982). Aspherical Earth structure from fundamental spheroidal-mode data. *Nature*, 298(5875), 609–613. <https://doi.org/10.1038/298609a0>
- Mavko, G., Mukerji, T., & Dvorkin, J. (2009). *The rock physics handbook: Tools for seismic analysis of porous media* (2nd ed.). Cambridge, UK: Cambridge University Press.
- McClain, J. S., Orcutt, J. A., & Burnett, M. (1985). The East Pacific Rise in cross section: A seismic model. *Journal of Geophysical Research*, 90(B10), 8627–8639. <https://doi.org/10.1029/JB090iB10p08627>
- McLaughlin, R. (1977). A study of the differential scheme for composite materials. *International Journal of Engineering Science*, 15(4), 237–244. [https://doi.org/10.1016/0020-7225\(77\)90058-1](https://doi.org/10.1016/0020-7225(77)90058-1)

- Menke, W., West, M., & Tolstoy, M. (2002). Shallow-crustal magma chamber beneath the axial high of the Coaxial segment of Juan de Fuca Ridge at the source site of the 1993 eruption. *Geology*, 30(4), 359–362. [https://doi.org/10.1130/0091-7613\(2002\)030<0359:SCMCBT>2.0.CO;2](https://doi.org/10.1130/0091-7613(2002)030<0359:SCMCBT>2.0.CO;2)
- Moser, T. J. (1991). Shortest path calculation of seismic rays. *Geophysics*, 56(1), 59–67. <https://doi.org/10.1190/1.1442958>
- Mura, T. (1987). *Micromechanics of defects in solids*, (2nd ed., revised edition). Dordrecht, The Netherlands: Martinus Nijhoff Publishers.
- Musgrave, M. J. (1970). Crystal acoustics: Introduction to the study of elastic waves and vibrations in crystal. San Francisco: Holden-Day.
- Nedimović, M. R., Carbotte, S. M., Diebold, J. B., Harding, A. J., Canales, J. P., & Kent, G. M. (2008). Upper crustal evolution across the Juan de Fuca Ridge flanks. *Geochemistry, Geophysics, Geosystems*, 9, Q09006. <https://doi.org/10.1029/2008GC002085>
- Newman, K. R., Nedimović, M. R., Canales, J. P., & Carbotte, S. M. (2011). Evolution of seismic layer 2B across the Juan de Fuca Ridge from hydrophone streamer 2-D traveltome tomography. *Geochemistry, Geophysics, Geosystems*, 12, Q05009. <https://doi.org/10.1029/2010GC003462>
- Purdy, G. M., & Detrick, R. S. (1986). Crustal structure of the Mid-Atlantic Ridge at 23°N from seismic refraction studies. *Journal of Geophysical Research*, 91(B3), 3739–3762. <https://doi.org/10.1029/JB091iB03p03739>
- Raitt, R. W. (1956). Seismic-refraction studies of the Pacific Ocean Basin: Part I: Crustal thickness of the central equatorial Pacific. *GSA Bulletin*, 67(12), 1623–1640. [https://doi.org/10.1130/0016-7606\(1956\)67\[1623:SSOTPO\]2.0.CO;2](https://doi.org/10.1130/0016-7606(1956)67[1623:SSOTPO]2.0.CO;2)
- Robigou, V., Delaney, J. R., & Stakes, D. S. (1993). Large massive sulfide deposits in a newly discovered active hydrothermal system, the High-Rise Field, Endeavour segment, Juan De Fuca Ridge. *Geophysical Research Letters*, 20(17), 1887–1890. <https://doi.org/10.1029/93GL01399>
- Seher, T., Crawford, W. C., Singh, S. C., Cannat, M., Combier, V., & Dusunur, D. (2010). Crustal velocity structure of the Lucky Strike segment of the Mid-Atlantic Ridge at 37°N from seismic refraction measurements. *Journal of Geophysical Research*, 115, B03103. <https://doi.org/10.1029/2009JB006650>
- Seher, T., Singh, S. C., Crawford, W. C., & Escartín, J. (2010). Upper crustal velocity structure beneath the central Lucky Strike segment from seismic refraction measurements. *Geochemistry, Geophysics, Geosystems*, 11, Q05001. <https://doi.org/10.1029/2009GC002894>
- Shearer, P. M. (1988). Cracked media, Poisson's ratio and the structure of the upper oceanic crust. *Geophysical Journal*, 92(2), 357–362. <https://doi.org/10.1111/j.1365-246X.1988.tb01149.x>
- Shearer, P. M., & Orcutt, J. A. (1986). Compressional and shear wave anisotropy in the oceanic lithosphere—The Ngendei seismic refraction experiment. *Geophysical Journal of the Royal Astronomical Society*, 87(3), 967–1003. <https://doi.org/10.1111/j.1365-246X.1986.tb01979.x>
- Sohn, R. A., Webb, S. C., Hildebrand, J. A., & Cornuelle, B. D. (1997). Three-dimensional tomographic velocity structure of upper crust, CoAxial segment, Juan de Fuca Ridge: Implications for on-axis evolution and hydrothermal circulation. *Journal of Geophysical Research*, 102(B8), 17,679–17,695. <https://doi.org/10.1029/97JB00592>
- Solomon, S. C., & Toomey, D. R. (1992). The structure of mid-ocean ridges. *Annual Review of Earth and Planetary Sciences*, 20(1), 329–366. <https://doi.org/10.1146/annurev.ea.20.050192.001553>
- Soule, D., Wilcock, W. S. D., Toomey, D. R., Hooft, E. E. E., & Weekly, R. T. (2016). Near-axis crustal structure and thickness of the Endeavour segment, Juan de Fuca Ridge. *Geophysical Research Letters*, 43, 5688–5695. <https://doi.org/10.1002/2016GL068182>
- Spudich, P., & Orcutt, J. (1980). Petrology and porosity of an oceanic crustal site: Results from wave form modeling of seismic refraction data. *Journal of Geophysical Research*, 85(B3), 1409–1433. <https://doi.org/10.1029/JB085iB03p01409>
- Stephen, R. A. (1985). Seismic anisotropy in the upper oceanic crust. *Journal of Geophysical Research*, 90(B13), 11,383–11,396. <https://doi.org/10.1029/JB090iB13p11383>
- Swift, S., Reichow, M., Tikku, A., Tominaga, M., & Gilbert, L. (2008). Velocity structure of upper ocean crust at Ocean Drilling Program Site 1256. *Geochemistry, Geophysics, Geosystems*, 9, Q10O13. <https://doi.org/10.1029/2008GC002188>
- Takei, Y. (2002). Effect of pore geometry on V_p/V_s : From equilibrium geometry to crack. *Journal of Geophysical Research*, 107(B2), 2043. <https://doi.org/10.1029/2001JB000522>
- Taylor, M. A. J., & Singh, S. C. (2002). Composition and microstructure of magma bodies from effective medium theory. *Geophysical Journal International*, 149(1), 15–21. <https://doi.org/10.1046/j.1365-246X.2002.01577.x>
- Telford, W. M., & Sheriff, R. E. (1990). *Applied geophysics*. Cambridge, UK: Cambridge University Press.
- Tong, C. H., White, R. S., Warner, M. R., & Grp, A. W. (2004). Effects of tectonism and magmatism on crack structure in oceanic crust: A seismic anisotropy study. *Geology*, 32(1), 25–28. <https://doi.org/10.1130/G19962.1>
- Toomey, D. R., Solomon, S. C., & Purdy, G. M. (1994). Tomographic imaging of the shallow crustal structure of the East Pacific Rise at 9°30' N. *Journal of Geophysical Research*, 99(B12), 24,135–24,157. <https://doi.org/10.1029/94JB01942>
- Tréhu, A. M. (1984). Lateral velocity variations in the Orozco transform fault inferred from observed incident angles and azimuths of P -waves. *Geophysical Journal International*, 77(3), 711–728. <https://doi.org/10.1111/j.1365-246X.1984.tb02217.x>
- Turcotte, D., & Schubert, G. (2014). *Geodynamics* (3rd ed.). Cambridge, UK: Cambridge University Press.
- Van Ark, E. M., Detrick, R. S., Canales, J. P., Carbotte, S. M., Harding, A. J., Kent, G. M., et al. (2007). Seismic structure of the Endeavour segment, Juan de Fuca Ridge: Correlations with seismicity and hydrothermal activity. *Journal of Geophysical Research*, 112, B02401. <https://doi.org/10.1029/2005JB004210>
- VanderBeek, B. P., Toomey, D. R., Hooft, E. E. E., & Wilcock, W. S. D. (2016). Segmentation of mid-ocean ridges attributed to oblique mantle divergence. *Nature Geoscience*, 9(8), 636–642. <https://doi.org/10.1038/ngeo2745>
- Vera, E. E., Mutter, J. C., Buhl, P., Orcutt, J. A., Harding, A. J., Kappus, M. E., et al. (1990). The structure of 0- to 0.2-m.y.-old oceanic crust at 9°N on the East Pacific Rise from expanded spread profiles. *Journal of Geophysical Research*, 95(B10), 15,529–15,556. <https://doi.org/10.1029/JB095iB10p15529>
- Walsh, J. B. (1968). Attenuation in partially melted material. *Journal of Geophysical Research*, 73(6), 2209–2216. <https://doi.org/10.1029/JB073i006p02209>
- Walsh, J. B. (1969). New analysis of attenuation in partially melted rock. *Journal of Geophysical Research*, 74(17), 4333–4337. <https://doi.org/10.1029/JB074i017p04333>
- Weekly, R. T., Wilcock, W. S. D., Hooft, E. E. E., Toomey, D. R., McGill, P. R., & Stakes, D. S. (2013). Termination of a 6 year ridge-spreading event observed using a seafloor seismic network on the Endeavour segment, Juan de Fuca Ridge. *Geochemistry, Geophysics, Geosystems*, 14, 1375–1398. <https://doi.org/10.1002/ggge.20105>
- Weekly, R. T., Wilcock, W. S. D., Toomey, D. R., Hooft, E. E. E., & Kim, E. (2014). Upper crustal seismic structure of the Endeavour segment, Juan de Fuca Ridge from traveltome tomography: Implications for oceanic crustal accretion. *Geochemistry, Geophysics, Geosystems*, 15, 1296–1315. <https://doi.org/10.1002/2013GC005159>
- White, R. S., & Stephen, R. A. (1980). Compressional to shear wave conversion in oceanic crust. *Geophysical Journal International*, 63(2), 547–565. <https://doi.org/10.1111/j.1365-246X.1980.tb02637.x>

- Wilcock, W. S. D., Archer, S. D., & Purdy, G. M. (2002). Microearthquakes on the Endeavour segment of the Juan de Fuca Ridge. *Journal of Geophysical Research*, 107(B12), 2336. <https://doi.org/10.1029/2001JB000505>
- Wilcock, W. S. D., & Delaney, J. R. (1996). Mid-ocean ridge sulfide deposits: Evidence for heat extraction from magma chambers or cracking fronts? *Earth and Planetary Science Letters*, 145(1), 49–64. [https://doi.org/10.1016/S0012-821X\(96\)00195-1](https://doi.org/10.1016/S0012-821X(96)00195-1)
- Wilcock, W. S. D., Hooft, E. E. E., Toomey, D. R., McGill, P. R., Barclay, A. H., Stakes, D. S., & Ramirez, T. M. (2009). The role of magma injection in localizing black-smoker activity. *Nature Geoscience*, 2(7), 509–513. <https://doi.org/10.1038/ngeo550>
- Wilkins, R. H., Fryer, G. J., & Karsten, J. (1991). Evolution of porosity and seismic structure of upper oceanic crust: Importance of aspect ratios. *Journal of Geophysical Research*, 96(B11), 17,981–17,995. <https://doi.org/10.1029/91JB01454>
- Woodward, R. L., & Masters, G. (1992). Upper mantle structure from long-period differential traveltimes and free oscillation data. *Geophysical Journal International*, 109(2), 275–293. <https://doi.org/10.1111/j.1365-246X.1992.tb00098.x>
- Wright, D. J. (1998). Formation and development of fissures at the East Pacific Rise: Implications for faulting and magmatism at mid-ocean ridges. In R. Buck, P. Delaney, J. A. Karson, & Y. Lagabrielle (Eds.), *Faulting and magmatism at mid-ocean ridges* (pp. 137–151). Washington, DC: American Geophysical Union.

Erratum

In the originally published version of this article, Table 2 was incorrectly typeset. The table has since been corrected, and this version may be considered the authoritative version of record.